NRL Memorandum Report 6405

Collisionless Tearing Instability of a Bi-Maxwellian Neutral Sheet with Exact Particle Orbits

G. R. BURKHART

Science Applications International Corporation
1710 Goodridge Dr.
McLean, VA 22102

JAMES CHEN

Geophysical and Plasma Dynamics Branch
Plasma Physics Division

March 27, 1989

SECURITY CLASSIFICATION OF THIS PAGE

REPORT DOCUMENTATION PAGE

Form Approved
OMB No 0704-0188

1a REPORT SECURITY CLASSIFICATION UNCLASSIFIED	1b RESTRICTIVE MARKINGS
2a SECURITY CLASSIFICATION AUTHORITY	3 DISTRIBUTION AVAILABILITY OF REPORT Approved for public release; distribution unlimited.
2b DECLASSIFICATION DOWNGRADING SCHEDULE	
4 PERFORMING ORGANIZATION REPORT NUMBER(S) NRL Memorandum Report 6405	5 MONITORING ORGANIZATION REPORT NUMBER(S)
6a NAME OF PERFORMING ORGANIZATION Naval Research Laboratory 6b OFFICE SYMBOL (If applicable) Code 4780	7a NAME OF MONITORING ORGANIZATION
6c ADDRESS (City, State, and ZIP Code) Washington, DC 20375-5000	7b ADDRESS (City, State, and ZIP Code)
8a NAME OF FUNDING/SPONSORING ORGANIZATION ONR & NASA 8b OFFICE SYMBOL (If applicable)	9 PROCUREMENT INSTRUMENT IDENTIFICATION NUMBER
8c ADDRESS (City, State, and ZIP Code) ONR, Arlington, VA 22203 NASA, Greenbelt, MD 20771	10 SOURCE OF FUNDING NUMBERS PROGRAM ELEMENT NO: 61153N; PROJECT NO: W-15-494; TASK NO:; WORK UNIT ACCESSION NO: DN880-024

11 TITLE (Include Security Classification)
Collisionless Tearing Instability of a Bi-Maxwellian Neutral Sheet with Exact Particle Orbits

12 PERSONAL AUTHOR(S)
Burkhart,* G.R. and Chen, J.

13a TYPE OF REPORT	13b TIME COVERED	14 DATE OF REPORT (Year, Month, Day)	15 PAGE COUNT
Interim	FROM _____ TO _____	1989 March 27	56

16 SUPPLEMENTARY NOTATION
*Science Applications International, McLean, VA 22102

17 COSATI CODES			18 SUBJECT TERMS (Continue on reverse if necessary and identify by block number)
FIELD	GROUP	SUB-GROUP	Collisionless tearing mode · Integrodifferential equation Anisotropic temperature Reconnection

19 ABSTRACT (Continue on reverse if necessary and identify by block number)

The tearing instability of a neutral sheet may be important to reconnection in the magnetosphere and elsewhere. The use of a bi-Maxwellian Harris equilibrium is broadly applicable to the physical environment and allows a continuous variation from isotropic to anisotropic situations. ~~We have solved~~ the integro-differential equation describing the linear tearing instability in the bi-Maxwellian neutral sheet without approximating the particle orbits. Results of this calculation are presented.

Comparison between the exact solution and the 3-region approximation[1] motivates the piecewise-straight-line approximation, a simplification which allows faster solution of the integro-differential equation, yet retains the important features of the exact solution.

20 DISTRIBUTION AVAILABILITY OF ABSTRACT ☒ UNCLASSIFIED/UNLIMITED ☐ SAME AS RPT ☐ DTIC USERS	21 ABSTRACT SECURITY CLASSIFICATION UNCLASSIFIED
22a NAME OF RESPONSIBLE INDIVIDUAL J.D. Huba	22b TELEPHONE (Include Area Code) (202) 767-3630 22c OFFICE SYMBOL Code 4780

DD Form 1473, JUN 86 Previous editions are obsolete SECURITY CLASSIFICATION OF THIS PAGE

S/N 0102-LF-014-6603

CONTENTS

COLLISIONLESS TEARING INSTABILITY OF A BI-MAXWELLIAN NEUTRAL SHEET WITH EXACT PARTICLE ORBITS

I Introduction

The collisionless tearing mode in a neutral sheet[2-5] has received considerable attention in the past two decades[6-10]. A neutral sheet can be described by a one-dimensional magnetic field $\mathbf{B}(z) = B_x(z)\hat{\mathbf{x}}$ such that B_x is odd in z, the coordinate normal to the plane of the sheet. A well-known model is the Harris equilibrium[11] which is established by balancing $\mathbf{J} \times \mathbf{B}$ and ∇p, where $\mathbf{J}(z) = J_y(z)\hat{\mathbf{y}}$ is in the plane of the neutral sheet. In its classic form[2,3] the instability is due to the finite mass of the current carriers, allowing the current sheet to filament ($\mathbf{k} = k_x\hat{\mathbf{x}}$) and attain a lower magnetic energy configuration. For this process, the existence of regions about $z = 0$ (the null plane) in which electrons and ions are essentially unmagnetized is critical. As the magnetic field is perturbed, an electric field is induced in the y direction, accelerating the unmagnetized electrons and ions. In our model, we will ignore the scalar potential. This instability is potentially important for magnetic reconnection processes that may occur in a number of physical systems such as the magnetotail[12,13] and in the day-side magnetopause[14,15]. In realistic physical systems, the magnetic field is generally not one dimensional. For example, the magnetotail would have a small B_z component and the magnetopause would have a B_y component comparable to the asymptotic B_x component. However, the instability occurring in a neutral sheet may be prototypical, elucidating the essential physics common to various configurations.

The majority of the previous papers on the collisionless tearing mode have used Maxwellian equilibrium distribution functions, for which the mode grows only slowly

Manuscript approved November 23, 1988.

($\gamma/\omega_{ci} \ll 1$). Applied to the earth's magnetotail, for example, this gives e-folding times which are significantly longer than the relevant time scales for possible reconnection except in extreme situations. For example, using the Harris equilibrium, Coppi et al.[6], estimated $\gamma \approx 1/5$ sec^{-1} - $1/15$ sec^{-1} with $\rho_i/\delta \approx 1$, where ρ_i is the asymptotic gyroradius, and δ is the magnetic scale length, which requires that the global bulk plasma flow across the tail be comparable to the thermal velocities. Such high-speed bulk flows are not necessarily observed prior to reconnection. However, it has been known that an electron temperature anisotropy can significantly affect the tearing instability growth rate. Forslund[16] showed that the mode was stabilized in equilibria with $(1 - T_{e\perp}/T_{e\|}) > \rho_e/\delta$. However, Laval and Pellat[17] later showed that these equilibria were unstable to a quickly growing obliquely propagating mode. A weak anisotropy $T_{e\perp} > T_{e\|}$ greatly increases the growth rate[16]. In addition, an anisotropic neutral sheet should be unstable to the Weible instability[18]. Thus, any electron anisotropy in the magnetotail plasma is likely to be non-linearly isotropized by these and other instabilities on much faster time scales than the typical time scale associated with reconnection in the magnetosphere. More recently, Chen and Palmadesso[1] investigated the dependence of the growth rate on the ion temperature anisotropy. They found that an ion temperature anisotropy could also enhance the tearing mode growth rate. For $T_{i\perp}/T_{i\|} \approx 1.2 - 1.5$, the growth rate was found to be one to two orders of magnitude greater than in the isotropic case. This was later confirmed by simulation results[19]. For small to moderate ion anisotropy $T_{i\perp}/T_{i\|} \sim 1.5$, the e-folding time can be reduced to a few minutes for the earth's magnetotail parameters, which is favorable in comparison with the observed

substorm onset time scales of tens of minutes. This suggests that non-Maxwellian features in the ion distribution function rather than in the electron distribution are of interest for magnetospheric processes. We do not expect a significant ion temperature anisotropy to be present in the quiescent magnetotail[20,21,22]. However, in a magnetotail-like geometry phase space is partitioned into disjoint subregions containing transient, chaotic, and integrable orbits[23]. Information of disturbances far from the current sheet would reach these subregions in different characteristic times, leading perhaps to non-Maxwellian features in the distribution function, a process referred to as "differential memory"[22] These non-Maxwellian features can persist on time scales of orbit diffusion across phase regions, a longer time than the e-folding time of the ion anisotropic tearing instability.

In works previous to and including ref. [1] the complicated particle orbits of the neutral sheet geometry have only been accounted for in approximate ways. One method of approximating the orbits is a global energy principle[5,7,24] computed to first order in the ratio of the Larmor radius to the magnetic scale length (the electron Larmor radius for an isotropic plasma). This method has the advantage that a particular form for the functional dependence of the perturbation on z is not assumed but the disadvantage that only a stability criterion may be found. A second method uses both approximate orbits and assumes a particular form for the eigenfunction. The most common example of the latter method is the two region approximation[6,8,10,25]. In this approximation all orbits within a nearby region of the field null are taken to be straight line orbits, and the eigenfunction of the field perturbation is assumed to be constant within that region (the "constant psi"

approximation). Outside of this region, the orbits are taken to be the usual drifting cyclotron orbits. Provided the ion distribution is isotropic and $(\rho_e/\rho_i) \ll 1$, where ρ_e and ρ_i are the Larmor radii of the electrons and ions, the ion contribution to the non-adiabatic perturbed current is small[6]. Thus, attention need only be paid to the crossing electron orbits.

An interesting facet of the work in ref. [1] was the identification of an ion-intermediate region within which the ion orbits were approximated by straight lines but the electron orbits were approximated by drifting guiding center orbits (the "3-region" approximation). This ion-intermediate region proved to be important in the ion anisotropic case; if the region was included the tearing mode growth rate increased by nearly an order of magnitude over a similar calculation where the ion contribution to the current outside of the electron inner region was taken to be negligible (the usual "2-region" approximation). It was therefore expected that the straight-line approximation for orbits within this large ion-intermediate region, as well as the "constant psi" approximation could be limiting for all but the smallest values of ρ_i in the presence of an ion anisotropy. Recently, Chen and Lee[26] have developed a method in which growth rates could be calculated taking into account all of the orbits exactly. This method removed the limitation in applicability arising from the constant-ψ approximation and from approximate orbits. They applied the treatment to a delta function particle distribution in perpendicular energy. This choice gave rise to a highly non-Maxwellian distribution function with a very fast growth rate, i.e. approaching the ion-cyclotron frequency. The eigenfunction was

highly structured within the electron inner region, so that the constant-ψ approximation would have been invalid. However, such a specialized distribution function is not likely to occur in physical systems, such as the magnetosphere; quantitative results require a more broadly applicable distribution function such as a bi-Maxwellian distribution function. In addition, their choice has not been previously analyzed by approximate linear theories, or by simulation, and there is no isotropic limit.

In this paper, we apply the integro-differential method of Ref. [26] to the bi-Maxwellian system. In addition to being more physical for the magnetotail, this model has the advantage that the equilibrium quantity $T_{i\perp}/T_{i||}$ is continuously variable so that it would be a better basis for a more complete study. We have solved the full integro-differential equation for the bi-Maxwellian neutral sheet with no restrictions on $T_{i\perp}/T_{i||}$ or ρ_i/δ. The solution shows that for $T_{i\perp}/T_{i||} > 1$ the growth is significantly enhanced and the maximum growth wavenumber k is increased in comparison with the isotropic case, in qualitative agreement with an earlier study (ref. [1] which used the 3-region approximation). However, the exact result reveals that the 3-region approximation underestimates the growth rate by a factor of two to five. This is found to be caused by incorrect classification of crossing and non-crossing orbits and by the constant-ψ approximation, which is taken in many approximate theories.

Although the integro-differential formalism can provide the exact answer, it is generally nontrivial to use. In particular, for complex systems, the orbit contributions for each matrix element may have to be evaluated repeatedly in order to

determine the dispersion relations, which may make the actual computation prohibitive. In this paper, we will describe a new approximate technique which is a simplified application of the full integro-differential treatment and which properly accounts for the essential features of orbit contributions. In particular, contributions from different types of orbits are properly taken into account and no assumption on ψ is necessary. This approximation allows much more efficient computation of matrix elements with minimal loss of overall accuracy. In order to fully understand the validity and advantages of this simplified integro-differential treatment, we will describe the the new approximation and its physical basis. In this connection, we will use the three-region approximation to illustrate the essential physics.

This paper will consist of two major components. In the first part (Secs. II and III), we will present the formulation and solution of the full integro-differential equation. In the second part (Secs. IV and V), we will discuss the reasons why previous approximations break down and describe a simplified integro-differential method which does not suffer from similar errors.

II Formulation

A Bi-Maxwellian, Neutral Sheet Equilibrium

A well known equilibrium exhibiting a neutral sheet is the Harris[11] equilibrium. For each species we choose a modified Harris equilibrium which includes a temperature anisotropy

$$f_0 = \frac{\hat{n}_0}{\pi^{1/2} v_{T_\parallel}} \exp[-H_\parallel/T_\parallel] F \tag{1}$$

where

$$F = \frac{\exp(-V^2/v_{T_\perp}^2)}{\pi v_{T_\perp}^2} \exp[-(H_\perp - V P_y)/T_\perp]. \tag{2}$$

Here $P_y = m v_y + (q/c) A_y(z)$, $H_\perp = m v_\perp^2/2$, $H_\parallel = m v_\parallel^2/2$, $T_\perp = m v_{T_\perp}^2/2$, $T_\parallel = m v_{T_\parallel}^2/2$, and V is an adjustable parameter representing the average velocity of the species under consideration. The subscripts "$\perp$" and "$\parallel$" refer to components perpendicular and parallel to the equilibrium magnetic field

$$\mathbf{B} = B_0 \tanh(z/\delta) \hat{\mathbf{e}}_\mathbf{x}. \tag{3}$$

The vector potential corresponding to this field is

$$A_y(z) = -B_0 \delta \ln\Big[\cosh(z/\delta)\Big]. \tag{4}$$

The relations

$$\frac{V_e}{T_{e\perp}} = -\frac{V_i}{T_{i\perp}}, \tag{5}$$

$$\frac{V}{v_{T_\perp}} = \frac{\rho}{\delta}, \tag{6}$$

are a result of the quasi-neutrality condition and Ampére's Law. Here ρ is the gyroradius in the asymptotic field, $\rho = v_{T_\perp}/\omega_c$ where $\omega_c = qB_0/mc$. As a consequence of these relations, we find the pressure profile

$$P(z) = \frac{B_0^2}{8\pi}\,\mathrm{sech}^2(z/\delta). \tag{7}$$

B The Fundamental Integro-Differential Equation

In this section we will briefly review the integro-differential equation for completeness' sake. The derivation is essentially the same as in[26], except that we have the simplification that $\partial f_0/\partial H_\parallel = (T_\perp/T_\parallel)\partial f_0/\partial H_\perp$.

As in the previous derivation, we take for the perturbed vector potential the usual tearing perturbation

$$\mathbf{A_1}(z,x,t) = \hat{\mathbf{e}}_\mathbf{y}\psi(z)e^{i(kx-\omega t)}. \tag{8}$$

The perturbed y-directional current is found to be

$$\begin{aligned}\frac{4\pi}{c}J_{1y}(z) &= \frac{1}{\delta^2}\sum_q \frac{2T_\perp}{T_{e\perp}+T_{i\perp}}\Bigg\{\mathrm{sech}^2(z/\delta)\psi(z) \\ &\quad + \int d^3v\left[1-\frac{kv_\parallel}{\omega}\left(1-\frac{T_\perp}{T_\parallel}\right)\right]\frac{f_0}{\hat{n}_0}\frac{v_y}{V}S_y\Bigg\},\end{aligned} \tag{9}$$

and Ampére's Law may be used to give a single equation for ψ

$$k^2\psi - \frac{\partial^2\psi}{\partial z^2} = \frac{4\pi}{c}J_{1y} \tag{10}$$

where S_y contains the integration over unperturbed orbits

$$S_y = i\omega\int_{-\infty}^{t} dt'\frac{v_y(z')}{V}\psi(z')e^{i(kv_\parallel-\omega)(t'-t)}. \tag{11}$$

In this configuration, particle motion is regular with a period that depends upon the constants of motion, $\mathcal{T}(H_\perp, P_y)$. Thus the quantity $v_y(z')\psi(z')$ may be expanded as a Fourier series in t'

$$v_y(z')\psi(z') = \sum_{n=0}^{\infty} \Phi_n e^{in\Omega(t'-t)},$$

where $\Omega = 2\pi/\mathcal{T}$. The Φ_n's are the Fourier coefficients at the current time t, that is

$$v_y(z)\psi(z) = \sum_{n=0}^{\infty} \Phi_n.$$

These may be found by an integration starting at the current time and extending over one period

$$\Phi_n = \frac{1}{\mathcal{T}} \int_t^{t+\mathcal{T}} dt'' \left[v_y(z'')\psi(z'') \right] e^{-in\Omega(t''-t)}.$$

Hence, we may write the identity

$$v_y(z')\psi(z') = \sum_n \left\{ \frac{1}{\mathcal{T}} \int_t^{t+\mathcal{T}} dt'' \left[v_y(z'')\psi(z'') \right] e^{-in\Omega(t''-t)} \right\} e^{in\Omega(t'-t)}.$$

We may now complete the t' integration in S_y to find

$$S_y = \sum_n \frac{-\omega}{\omega - n\Omega - kv_\parallel} \frac{1}{\mathcal{T}} \int_t^{t+\mathcal{T}} dt'' \left[\frac{v_y(z'')}{V} \psi(z'') \right] e^{-in\Omega(t''-t)}$$

Thus we have replaced the integration over an infinite number of orbits with a sum over an infinite number of harmonics of the orbital period. Physically, we know that the higher harmonics $n \neq 0$ correspond to resonances between the orbital motion and the oscillation of the eigenfunction. Resonances with the higher harmonics may be discarded if the frequency of the fields is much less than the frequency of the orbit, $\omega \ll \Omega$ for all P_y and $H_\perp$. When the orbits correspond to cyclotron motion,

this is identical to the low frequency approximation. In this formulation, we will assume that all contributions from resonances with higher harmonics are negligible, and therefore we ignore all of the terms but $n = 0$.

$$S_y = \frac{-\omega}{\omega - kv_{\|}} \frac{1}{\mathcal{T}} \int_t^{t+\mathcal{T}} dt' \Big[\frac{v_y(z')}{V} \psi(z') \Big]. \tag{12}$$

In the last equation we have reduced the double prime to a single prime for convenience. Our manipulations upon S_y have separated the parallel direction from the perpendicular direction. Now, we may complete the parallel velocity integral in the perturbed current

$$\begin{aligned} \frac{4\pi}{c} J_{1y} &= \frac{1}{\delta^2} \sum_q \frac{2T_\perp}{T_{i\perp} + T_{e\perp}} \Big\{ \operatorname{sech}^2(z/\delta)\psi(z) \\ &\quad + \Big[\xi Z(\xi) + \Big(1 - \frac{T_\perp}{T_{\|}} \Big) \Big(1 + \xi Z(\xi) \Big) \Big] Q(z) \Big\}, \end{aligned} \tag{13}$$

where

$$Q(z) = \int d^2v \, \frac{v_y}{V} F \, \frac{1}{\mathcal{T}} \int_t^{t+\mathcal{T}} dt' \Big[\frac{v_y(z')}{V} \psi(z') \Big] \tag{14}$$

$\xi = \omega / kv_{\|}$, and Z is the plasma dispersion function. The integration over one orbital period may be replaced by an integration along the path of the orbit. Thus

$$Q(z) = \int d^2v \, \frac{v_y}{V} F \, \frac{1}{\mathcal{T}} \oint \frac{dz'}{|v_z(z')|} \Big[\frac{v_y(z')}{V} \psi(z') \Big]. \tag{15}$$

The period is given by

$$\mathcal{T} = \oint \frac{dz'}{|v_z(z')|}.$$

C Method of Solution

The general numerical method used here is a reduction of the integro-differential equation to a matrix equation, and then a numerical solution of the eigenvalue equation for the growth rate. Such a method was used in ref. [26] so we will only touch on this briefly. For further details see refs. [26,27]. In our case, however, we found that we could reduce the computation time for each matrix element significantly by changing the order of integration, and we will discuss this change in some detail.

As in ref. [26], the numerical solution of Eq. (10) with Eq. (13) is found by representing the eigenfunction $\psi(z)$ as a sum over basis functions

$$\psi(z) = \sum_n a_n \phi_n(z).$$

Multiplying Eq. (10) by a basis function, ϕ_m and integrating over all z we obtain

$$0 = \sum_n a_n G_{nm} \tag{16}$$

where the matrix elements

$$\begin{aligned} G_{nm} &= k^2 \int dz\, \phi_n \phi_m + \int dz\, \frac{\partial \phi_n}{\partial z} \frac{\partial \phi_m}{\partial z} - \frac{2}{\delta^2} \int dz\, \mathrm{sech}^2(z/\delta) \phi_n \phi_m \\ &\quad - \frac{2}{\delta^2} \sum_{species} \frac{T_\perp}{T_{\perp i} + T_{\perp e}} \left[\xi Z(\xi) + \left(1 - \frac{T_\perp}{T_\parallel}\right)\left(1 + \xi Z(\xi)\right) \right] K_{mn} \end{aligned} \tag{17}$$

and

$$K_{mn} = \int dz\, \phi_m(z) \int d^2v\, \frac{v_y}{V} F\, \frac{1}{T} \oint \frac{dz'}{|v_z(z')|} \left[\frac{v_y(z')}{V} \phi_n(z') \right]. \tag{18}$$

We solve Eq. (16) numerically by first solving the eigenvalue equation

$$\lambda a_m = \sum_n a_n G_{mn}$$

and then searching for a frequency root of the dispersion relation

$$\lambda(\omega, k) = 0. \tag{19}$$

In order to find the parameters upon which K_{mn} depends, we find it convenient to normalize our variables. When occurring within the integration of K_{mn}, time will be scaled to the cyclotron period in the asymptotic field. Thus for the orbital period,

$$\hat{T} = \omega_c T.$$

Distance will be scaled throughout to the magnetic scale length δ. Thus,

$$\hat{z} = z/\delta \qquad \text{and} \qquad \hat{k} = k\delta.$$

The velocities are then scaled by

$$\hat{v} = v/\omega_c\delta.$$

Note that the quantity v_y/V becomes $\hat{v}_y(\delta/\rho)^2$. We also scale the constants of motion $H_\perp$ and P_y so that

$$h = H_\perp/(\frac{m}{2}\delta^2\omega_c^2)$$

and

$$p = P_y/(m\delta\omega_c)$$

are only dependent upon $\hat{v}_y$, $\hat{v}_z$, and $\hat{z}$. The quantity K_{mn} becomes

$$K_{mn} = \frac{\delta}{\pi}(\delta/\rho)^6 \exp[-(\rho/\delta)^2]\hat{K}_{mn}$$

where

$$\hat{K}_{mn} = \int d\hat{z}\, \phi_m(\hat{z}) \int d^2\hat{v}\, \hat{v}_y \hat{F}\, \frac{1}{\hat{T}} \oint \frac{d\hat{z}'}{|\hat{v}_z(z')|}\, \hat{v}_y(\hat{z}')\phi_n(\hat{z}')$$

and

$$\hat{F} = \exp[-(\delta/\rho)^2 h + 2p].$$

Thus $\hat{K}_{mn}$ is a function of ρ/δ only. The matrix elements $\hat{K}_{mn}$ must be calculated for each species using the appropriate gyroradius ρ_i or ρ_e. However, they need not be calculated anew for a change in any other parameter such as frequency, wavenumber, or temperature anisotropy. This property may not be preserved in other geometries.

We now restrict the problem to a consideration of only symmetric solutions. Thus, we only need perform the $\hat{z}$ and $\hat{z}'$ integrations over contributions in the first quadrant. Therefore, we write, after a change in the order of integration

$$\begin{aligned} \hat{K}_{mn} \;=\; & \int_0^\infty dh\, e^{-(\delta/\rho)^2 h} \int_{-\infty}^{\sqrt{h}} dp\, e^{2p} \\ & \times \frac{g(p,h)}{\hat{T}} \left[2\int_{z_1}^{z_2} dz\, \frac{\hat{v}_y(z)}{|\hat{v}_z(z)|}\phi_m(z)\right]\left[2\int_{z_1}^{z_2} dz'\, \frac{\hat{v}_y(z')}{|\hat{v}_z(z')|}\phi_n(z')\right] \end{aligned} \qquad (20)$$

where

$$g(p,h) = \begin{cases} 1 & p < -\sqrt{h} \\ 2 & \sqrt{h} > p \geq -\sqrt{h}. \end{cases}$$

The turning points z_1 and z_2 are determined by $\hat{v}_z = 0$ and are given by

$$z_1 = \begin{cases} \text{Arccosh}\left\{\exp\left[-\sqrt{h} - p\right]\right\} & p < -\sqrt{h} \\ 0 & \sqrt{h} > p \geq -\sqrt{h} \end{cases}$$

and

$$z_2 = \mathrm{Arccosh}\Big\{\exp\Big[\sqrt{h} - p\Big]\Big\}.$$

Note that the value $p = -\sqrt{h}$ unambiguously distinguishes between crossing ($-\sqrt{h} \leq p < \sqrt{h}$) and non-crossing ($p < -\sqrt{h}$) orbits.

The factor $g(p,h)$ is due to the distinction between crossing and non-crossing orbits. This can be explained as follows. For non-crossing orbits, Fig. 1 shows the regions of integration in the $\hat{z} - \hat{z}'$ plane for two cases of the momentum and a sample value of the energy. The gray shaded regions are the areas of integration for the value $p = -\sqrt{h} - \epsilon$ as $\epsilon \to 0$. For ϵ sufficiently small, non-crossing orbits can come arbitrarily close to the null plane. The cross-hatched regions are the areas of integration for a smaller value of the momentum ($p < -\sqrt{h}$) such that the orbital turning points are at $\hat{z} = z_1$ and z_2. Further decreases in the momentum $p \to -\infty$ lead to farther separation in the two areas of integration, the top area tending to $\hat{z} = \hat{z}' = \infty$ and the bottom area to $\hat{z} = \hat{z}' = -\infty$. There is no region of integration in the second and fourth quadrants ($\hat{z}\hat{z}' < 0$) because no non-crossing orbit passes through two planes with z-coordinate $\hat{z}$ and $\hat{z}'$ that are on different sides of the null plane. For crossing orbits, Fig. 2 shows regions of integration. The interior of the larger square (the gray shaded area plus the cross-hatched area) represents the area of integration with the largest value of momentum corresponding to a crossing orbit, $p = -\sqrt{h}$. Further increases in the momentum lead to decreased areas of integration, such as the the cross-hatched area shown, until the area shrinks to zero for $p = \sqrt{h}$, which is the largest value of the momentum kinematically allowed.

Imposing symmetry in $\hat{z}$, only the quadrant with both $\hat{z}$ and $\hat{z}'$ greater than zero need be included in the integration, and therefore we simply must multiply the crossing orbit contribution by a factor of four and the non-crossing orbit contribution by a factor of two. The crossing orbit contribution is thus weighted by an additional factor of two. For odd modes (in $\hat{z}$), the factor $g(p,h)$ is unity for non-crossing orbits and zero for crossing orbits.

Equation (20) has three desirable properties: it is symmetric under interchange of m and n, neither of the coordinates z and z' is preferred, and for $m = n$, the result, K_{mn}, is positive definite. Numerically, Eq. (20) only requires three nested integrations since the $\hat{z}$ and $\hat{z}'$ integrations may be performed independently. This represents a substantial savings in computer time and accuracy over the form used in ref. [26] which requires four nested integrations.

D Implementation

The basis functions which we have chosen are the chapeau functions,

$$\phi_m = \begin{cases} (\hat{z} - \hat{z}_{m-1})/(\hat{z}_m - \hat{z}_{m-1}) & \hat{z}_{m-1} \le \hat{z} \le \hat{z}_m \\ (\hat{z}_{m+1} - \hat{z})/(\hat{z}_{m+1} - \hat{z}_m) & \hat{z}_m \le \hat{z} \le \hat{z}_{m+1} \\ 0 & \text{otherwise} \end{cases}$$

except for the last basis function at $\hat{z}_N \gg 1$

$$\phi_N = \begin{cases} (\hat{z} - \hat{z}_{N-1})/(\hat{z}_N - \hat{z}_{N-1}) & z_{N-1} \le z \le z_N \\ 0 & \text{otherwise} \end{cases}$$

and the basis function at the neutral plane,

$$\phi_1 = \begin{cases} (\hat{z} - \hat{z}_1)/\hat{z}_1 & 0 \le z \le z_1 \\ 0 & \text{otherwise.} \end{cases}$$

The primary advantage offered by these chapeau functions is that the center points need not be regularly spaced. Thus in the asymptotic region where $\psi \sim \exp(-\hat{k}\hat{z})$ we may place the basis function centers far apart. We tested the sensitivity of our code to the number of basis functions by doubling this number to the present value (100) using a mode with a slow exponential decay in the asymptotic region ($\hat{k} = 0.1$) compared to the fastest growing mode. Such an increase changed the computed frequency by less than 5%. This suggests that the code is capable of finding very extended eigenfunctions with good accuracy.

Actually, the worst accuracy limitation arose in the matrix solver (single precision on a 32-bit computer), which requires some diagonality to solve very large matrices. For large ρ_i, however, the large ion orbits make the matrix K_{mn} very non-diagonal, and therefore G_{mn} becomes non-diagonal. Since, in the routine we used, the accuracy of the computed eigenvalues is decreased as the matrix becomes less diagonal, the frequencies computed by our method are less accurate for larger values of ρ_i/δ. In practice, this led to an inaccuracy of around 2% in computed values of the frequency for $\rho_i/\delta = 1/2$.

III Results

We have solved the full integro-differential equation Eq. (10) by solving the equivalent matrix equation Eq. (16) using exact equilibrium orbits. In Fig. 3, the solid line is the solution of the dispersion relation [Eq. (19)] for the isotropic temperature case ($T_{i\perp}/T_{i\|} = 1$) with $\rho_i/\delta = 1/10$. The dashed line is the 3-region result for the same parameters. In this isotropic case, the 3-region approximation gives nearly the same result as the classical 2-region approximation as shown in Ref. [1], and we see that the previous approximation agrees well with the exact solution. However, it has been shown that even small to moderate deviations from exact ion temperature isotropy can cause the 2-region approximation to break down; inclusion of the ion-intermediate region can lead to a one to two order of magnitude increase in growth rate[1] In Fig. 4, we show the case for $T_{i\perp}/T_{i\|} = 1.2$ with $\rho_i/\delta = 1/10$. The solid line again is the exact solution and the dashed line is the 3-region result. The peak growth rate of the exact solution is roughly five times greater than that of the 3-region approximation and the marginal wavenumber is significantly greater than the approximate result. We emphasize that the 2-region approximation is already completely invalid in this region, giving growth rates one to two orders of magnitude lower than that indicated by the dashed-line 3-region result. Clearly, the 3-region approximation which included the ion-intermediate region provided significant improvement over the conventional approximations, but evidently still fell far short of the exact solution. The shortcoming of the 3-region approximation can be traced to the fact that the different types of orbits, crossing and non-crossing, are incorrectly

accounted for in the inner and outer regions and that the eigenfunction ψ is assumed to be constant in the electron-inner region and ion-intermediate region. These are two aspects of the problem that cannot be easily dealt with approximately so that an integro-differential approach is necessary. In Sec. V, we will discuss these issues in greater detail in formulating a simple method of solving the integro-differential equation while correctly taking into account the essential physics.

In Fig. 5, we have plotted (solid lines) the peak growth rate versus $T_{i\perp}/T_{i||}$ for several values of ρ_i/δ. The short and long dashed lines represent a number of approximations and will be discussed later (Sec. V). The solid curve "a" is the case $\rho_i/\delta = 1/2$, curve "b" corresponds to $\rho_i/\delta = 1/10$ and curve "c" is $\rho_i/\delta = 1/100$. Because of the approximate scaling $\gamma/\omega_{ci} \sim (\rho_i/\delta)^{5/2}$ in the isotropic limit[1] the growth rate is greater for larger ρ_i/δ. However, at a moderate temperature anisotropy, $T_{i\perp}/T_{i||} - 1 > \rho_i/\delta$, the growth rate scales as an inverse power of ρ_i/δ. (The approximate theory has the growth rate scaling of ρ_i/δ in this regime.) For small values of ρ_i/δ the transition between these two regimes of anisotropy occurs at smaller anisotropies, so that the growth is enhanced more quickly as the anisotropy is increased in this regime of ρ_i. Thus, curve "a" shows the least variation and curve "c" shows the most variation as $T_{i\perp}/T_{i||}$ is increased. For curve "c" the growth rate increases by nearly four orders of magnitude as $T_{i\perp}/T_{i||}$ increases from exact isotropy to 1.5.

Figure 6 shows the peak wavenumber versus $T_{i\perp}/T_{i||}$ for the examples shown in Fig. 5. Again, the solid curves represent the exact solution and the short and

long dashed lines are approximate results to be discussed later. For the present discussion, the important point is that the wavenumber corresponding to maximum growth increases with increasing $T_{i\perp}/T_{i\|}$, favoring shorter wavelength modes. This effect is also stronger for smaller ρ_i/δ. The results of the 3-region approximation (short dashed lines) are in qualitative agreement with the exact result but, as with the dispersion relation, essential quantitative disagreement develops except for relatively small degrees of anisotropy.

We have seen that the collisionless tearing mode in a neutral sheet requires solution of an integro-differential equation except for limited parameter values ($.5 \gtrsim \rho_i/\delta \gtrsim .05$ and $T_{i\perp}/T_{i\|} - 1 \lesssim .5\rho_i/\delta$). However, the integro-differential treatment is highly non-trivial even for the relatively simple system given here. For more complex systems, such as the sheared magnetic field geometry, solution of the full integro-differential equation may be prohibitive in terms of the necessary computation. It is, therefore, desirable to devise a method which provides a solution of the integro-differential equation without sacrificing accuracy and validity. In the following sections, we will describe a method using a new piecewise-straight-line approximation of crossing orbits in evaluating the matrix elements. It is important to point out that this method still solves the integro-differential equation, but the time required for computation of the matrix elements can be reduced significantly, allowing for solution of the problem in complex systems.

In order to understand the physical basis for the method, we will use the 3-region consideration to illustrate the essential physics required. Then we will apply the

new simplified treatment to the bi-Maxwellian tearing mode problem solved in the preceding sections to demonstrate its validity for a wide range of parameter values.

IV Review of the "3-Region" Approximation

We briefly review the "3-region" approximation of Chen and Palmadesso[1], which has been used to discuss the ion anisotropic tearing mode. In this approximation, the sheet is divided into three regions; 1.) the electron-inner region, $|z| < d_e$, within which both the electrons and ions are modeled by free trajectories, 2.) the ion-intermediate region, $d_e < |z| < d_i$, where the electrons are magnetized but ions still have free trajectories, and 3.) the outer region, $|z| > d_i$ where both species are magnetized. The parameters d_i and d_e are chosen to be

$$d_e = \sqrt{2|\rho_e|/\delta} \qquad d_i = \sqrt{\rho_i/(2\delta)}.$$

The position $\hat{z} = d_e$ is the turning point of the axis crossing electron orbit with $p = 0$, in the limit $\rho_e \ll 1$, and d_i is one half the turning point of the orbit with $p = 0$.

In the electron inner region the current is taken to be

$$J_{1y} = J_{ad} + J_e^< + J_i^<.$$

In the ion-intermediate region, we have

$$J_{1y} = J_{ad} + J_e^> + J_i^<,$$

and in the outer region

$$J_{1y} = J_{ad} + J_e^> + J_i^>.$$

Here, the adiabatic current is

$$J_{ad} = 2\frac{c}{4\pi\delta^2}\,\mathrm{sech}^2(\hat{z}), \tag{21}$$

For each species, the inner region current is

$$J^{<} = \frac{c}{4\pi\delta^2}\frac{2T_\perp}{T_{\perp i}+T_{\perp e}}\left[\xi Z(\xi)+\left(1-\frac{T_\perp}{T_\parallel}\right)\left(1+\xi Z(\xi)\right)\right] \times\left(\frac{1}{2}\frac{\delta^2}{\rho^2}+1\right)\int_{-d}^{d}d\hat{z}'\psi(\hat{z}'), \tag{22}$$

and the outer region current is

$$J^{>} = -\frac{c}{4\pi\delta^2}\frac{2T_\perp}{T_{\perp i}+T_{\perp e}}\left[\xi Z(\xi)-\left(1+\frac{T_\perp}{T_\parallel}\right)\left(1+\xi Z(\xi)\right)\right] \times\left(1+\frac{1}{2}\frac{\rho^2}{\delta^2}\right)\frac{\mathrm{sech}^4(\hat{z})}{\tanh^2(\hat{z})}\psi(\hat{z}). \tag{23}$$

Had we included the density profile $\mathrm{sech}^2(\hat{z})$ in writing Eq. (22), the resulting matrix elements, K_{mn}, would be proportional to $\int_{-d}^{d}d\hat{z}\,\phi_m(\hat{z})\,\mathrm{sech}^2(\hat{z})\int_{-d}^{d}d\hat{z}'\,\phi_n(\hat{z}')$. Such a non-symmetric matrix is undesirable on both physical and computational grounds (the eigenvalues of the integro-differential operator, and also of the matrix G_{mn} must be real[27]. The lack of symmetry arises because the straight-line model orbits in the inner region are inconsistent with an equilibrium $\mathrm{sech}^2(\hat{z})$ pressure profile. We must therefore take a uniform pressure profile.

However, if a differential equation approximation is desired (as in ref. [1]), we may take the constant-ψ approximation for the integral $\int_{-d}^{d}d\hat{z}'\psi(\hat{z}')$. Then there is no problem with retaining the physical pressure profile, and the inner region current may be written as

$$J^{<} = \frac{c}{4\pi\delta^2}\frac{2T_\perp}{T_{\perp i}+T_{\perp e}}\left[\xi Z(\xi)+\left(1-\frac{T_\perp}{T_\parallel}\right)\left(1+\xi Z(\xi)\right)\right]\left(\frac{1}{2}\frac{\delta^2}{\rho^2}+1\right)\mathrm{sech}^2(\hat{z})\psi(\hat{z}). \tag{24}$$

Therefore, if we model the inner region orbits as straight lines, we must either take the constant-ψ approximation, or we must use a constant pressure profile. This

restriction applies because the inner region is entirely composed of crossing orbits in this approximation. When we discuss the piecewise-straight-line approximation, which does not have an inner region or outer region as such, we need not be concerned about the consistency between the orbits and the density profile.

V Features of the Exact Solution and Comparison to the 3-Region Approximation

An important diagnostic of the integro-differential equation is the effective potential, defined by

$$V_{eff}(\hat{z})\psi(\hat{z}) = -\frac{4\pi\delta^2}{c} J_{1y}(\hat{z})$$

so that the integro-differential equation takes the form of the Schrödinger equation

$$\frac{\partial^2\psi}{\partial\hat{z}^2} - (V_{eff}(\hat{z}) - E)\psi = 0,$$

where $E = -\hat{k}^2$. The approximate 3-region effective potential we have used is given by

$$V_{eff}(\hat{z}) = \begin{cases} V_0 + V_e^< + V_i^< & 0 \le |\hat{z}| \le d_e \\ V_0 + V_i^< + V_e^> & d_e < |\hat{z}| \le d_i \\ V_0 + V_i^> + V_e^> & d_i < |\hat{z}|, \end{cases} \tag{25}$$

where

$$V_0 = -2\,\mathrm{sech}^2(\hat{z}), \tag{26}$$

$$V_e^< = \frac{2T_{\perp e}}{T_{\perp i} + T_{\perp e}} \xi_e Z(\xi_e)\left(\frac{1}{2}\frac{\delta^2}{\rho_e^2} + 1\right)\mathrm{sech}^2(\hat{z}), \tag{27}$$

$$V_e^> = \frac{2T_{\perp e}}{T_{\perp i} + T_{\perp e}} \xi_e Z(\xi_e)\left(1 + \frac{1}{2}\frac{\rho_e^2}{\delta^2}\right)\frac{\mathrm{sech}^4(\hat{z})}{\tanh^2(\hat{z})}, \tag{28}$$

$$V_i^< = \frac{2T_{\perp i}}{T_{\perp i} + T_{\perp e}}\left[\xi_i Z(\xi_i) + \left(1 - \frac{T_{\perp i}}{T_{\|i}}\right)\left(1 + \xi_i Z(\xi_i)\right)\right]\left(\frac{1}{2}\frac{\delta^2}{\rho_i^2} + 1\right)\mathrm{sech}^2(\hat{z}) \tag{29}$$

and

$$V_i^> = \frac{2T_{\perp i}}{T_{\perp i} + T_{\perp e}}\left[\xi_i Z(\xi_i) + \left(1 - \frac{T_{\perp i}}{T_{\|i}}\right)\left(1 + \xi_i Z(\xi_i)\right)\right]\left(1 + \frac{1}{2}\frac{\rho_i^2}{\delta^2}\right)\frac{\mathrm{sech}^4(\hat{z})}{\tanh^2(\hat{z})}, \tag{30}$$

This potential is found by dividing the current [Eqs. (21),(24), and (23)] by $\psi(\hat{z})$. In Fig. 7, we show the effective potential for a solution of the integro-differential equation (solid line) together with the a the 3-region approximation to the effective potential (dashed line) for an isotropic example. Although the overall shapes of the exact and approximate potentials are quite similar, important differences exist both within the electron-inner region and in the ion-intermediate region. For isotropic plasmas, we will find, the most important differences between the exact and approximate potentials are due to the response of electron crossing orbits and occur within the electron-inner region. The differences between the two potentials which exist in the ion-intermediate region will be found to be of less importance to the isotropic tearing instability, but of major importance to the anisotropic instability.

An enlargement of Fig. 7, which shows the details of the ion-intermediate region potential, is shown in Fig. 8. The straight long-dashed line is the level $E = -k^2$. In the exact effective potential, there are additional features not given by Eq. (25). Specifically, there is a negative spike in the exact potential, located just outside of the electron inner region, which is due to the contribution of figure-8 electron orbits. (Orbits such that $0 > p > -\sqrt{h}$ make a figure "8" in the reference frame moving with the drift speed of the orbit.) Such orbits are not fully accounted for by the straight-line approximation. Also, the ion crossing orbit contribution is extended to greater values of $\hat{z}$ than in the approximate potential. (This contribution appears as the difference between the solid line and the short dashed lane from $\hat{z} = d_i$ to $\hat{z} \approx 0.6$.) This is due to the crossing ions which have energies greater than the thermal energy.

The effective potential curve for an approximation may be used to assess the inaccuracy in the eigenfunction solution. The area between the approximated and exact potential curves relative to the total area between the exact potential curve and the energy, $E = -k^2$, is a measure of the inaccuracy incurred in using the particular approximation. In addition, the inaccuracy attributable to a particular type of orbits can be evaluated by calculating the area difference due to the orbits in question. Features in Fig. 8, specifically the negative spike due to electron figure-8 orbits and the contribution from the high energy ion orbits are found to be unimportant in the isotropic case.

Of much greater importance is the difference between the exact potential and the approximate potential within the electron inner region, as was shown in Fig. 7. The constant-ψ approximation is probably the origin of the large difference between the potential of the 3-region approximation and the exact potential in the electron-inner region. In reality, since the potential is much larger than than the energy the eigenfunction is strongly evanescent in the electron-inner region and not at all constant. The physical interpretation is this: Rather than a uniform perturbed current density forming throughout the electron-inner region, actually strong "skin" currents form at the edge of the inner region as a response to the induced electric field $E_y = \gamma\psi/c$. However, a certain amount of total current is required within the electron inner region to maintain the magnetic field perturbation, and this total current is now seen to be carried by the thin "skin" current, rather than by a uniform current density. Thus the induced electric field must be larger than the constant-ψ approximation would lead us to believe, implying a larger growth rate.

Therefore, we see that the constant-ψ approximation under estimates the growth rate because it does not account for the current density gradient in the inner region.

The growth rate for the isotropic case, $\rho_i/\delta = 1/10$, as a function of $\hat{k}$ is given in Fig. 3. Although the 3-region approximation (dashed line) under estimates the growth rate, as has been predicted, the approximation does much better here than in some cases we will discuss presently.

In the anisotropic case, shown in Fig. 4, the agreement of the 3-region approximation with the exact solution is not nearly so good. Here, the peak growth of the exact solution is about four times the peak of the 3-region approximation and unlike in the isotropic case, the 3-region approximation now over estimates the wavenumber corresponding to the peak of the growth rate.

The effective potential for the fastest growth eigenfunction in Fig. 4 is shown in Fig. 9. The minimum value of the effective potential in the ion-intermediate region is roughly given by the 3-region approximation, which for these parameters scales with $1 - T_{i\perp}/T_{i\|}$, however, important differences exist in the shapes of these two potentials. For ρ_i/δ small, as in this case, the contribution from non-crossing orbits is small. The contribution to the potential from the crossing orbits is therefore the difference between V_{eff} and the adiabatic potential $V_0 = \mathrm{sech}^2(\hat{z})$; in the 3-region approximation, this difference is given by $V^<$. It is important to note that in the anisotropic case the contribution from the ion crossing orbits has changed sign, and again extends to larger values of $\hat{z}$ than the 3-region approximation indicates. Further, the contribution has increased in absolute value, so that the area between

the exact and approximate potential in the ion-intermediate region is comparable to the total area between the exact potential and the energy. Thus, the differences between the exact and approximate potentials due to the ion crossing orbits dominate, rather than differences due to electron crossing orbits which dominate in the isotropic case.

The effect of increasing the ion temperature anisotropy on the ψ eigenfunction is shown in Fig. 10 (these are the eigenfunctions corresponding to the maximum growth rate). As the anisotropy is increased the eigenmode appears to becomes more strongly trapped in the ion-intermediate region potential well, which becomes deeper. Because the eigenfunction becomes more trapped in the ion-intermediate region, constant-ψ approximation breaks down inside of $|\hat{z}| = d_i$.

To summarize the comparison between the isotropic and anisotropic case, in the anisotropic case the ion contribution to the effective potential $(V_{eff} - V_0)$ in the ion-intermediate region has changed sign and the difference between the ion-intermediate region potential well and the adiabatic potential well is greater than in the isotropic case. Thus the difference between the potential of the three region approximation and the potential of the the exact solution in the ion-intermediate region will become more important as the anisotropy is increased. This difference is primarily due to the inclusion into the exact potential of the contribution of high energy crossing orbits. Further, the constant-ψ approximation of the 3-region approximation will be less valid as the anisotropy is increased.

Returning to Figs. 5 and 6, we can see that as the temperature anisotropy is

increased, the 3-region approximation (dashed line) disagrees more with the exact solution (solid line). Also, as ρ_i/δ is decreased, the disagreement of the 3-region approximation becomes greater. As we can see from the effective potential, shown in Fig. 11, as ρ_i/δ is decreased, the contribution to the effective potential from crossing orbits, especially the electron crossing orbits, is increased. Thus, as ρ_i/δ is decreased, the role of the electron inner region "skin" currents discussed earlier becomes greater and the constant-ψ approximation becomes more invalid. Thus we have the rather surprising result that as ρ_i/δ is decreased, the constant-ψ approximation is less valid.

The dashed line, which agrees with the solid line much better, especially in the large ρ_i ($\rho_i/\delta = 1/2$) and in the small ρ_i ($\rho_i/\delta = 1/100$) cases, gives the frequency solution of our piecewise-straight-line approximation.

A A piecewise-straight-line approximation

We have solved the integro-differential equation in the neutral sheet geometry without approximating the particle orbits or the perturbed potential eigenfunction, and the results show that in much of parameter space either the constant-ψ approximation is invalid or the approximate orbits as in the 3-region approximation are not valid. Computation of the K_{mn} matrix elements, however, is time consuming. In fact, if the matrix elements depended upon more than a single parameter, as they fortunately do in this geometry, the problem would not be practical to solve in this way. In more complicated geometries, such as the sheared field geometry, the matrix elements would not only be more complicated to compute, but they

would have to be recomputed more frequently to perform a parameter search. In the sheared field geometry, for example, the matrix elements would also depend upon the wavenumber as well as the dependence upon the asymptotic gyroradius.

The essentials of the full integro-differential equation is that no form for the perturbed potential eigenfunction is assumed, such as the constant-ψ approximation, and that orbits are treated as crossing or non-crossing depending upon the values of the azimuthal momentum and the energy, rather than the position $\hat{z}$. The adverse impact of approximating crossing orbits by straight lines seems to be smaller.

Therefore, we have approximated the orbit integration over a basis function by assuming that the velocity is roughly constant over that basis function

$$\int_{z_1}^{z_2} d\hat{z}' \, \frac{\hat{v}_y(\hat{z}')}{|\hat{v}_z(\hat{z}')|} \phi_n(\hat{z}') \approx \frac{\hat{v}_y(\hat{z}_n)}{|\hat{v}_z(\hat{z}_n)|} \int_{z_{min}}^{z_{max}} d\hat{z}' \, \phi_n(\hat{z}')$$

provided the orbit is a crossing orbit. Here, z_{min} and z_{max} are the minimum and maximum extents of the chapeau basis function centered at $\hat{z}_n$. If the turning point occurs within the basis function, however, the contribution from that orbit is discarded. It would also be straightforward to include the contribution from the turning point in some approximate way. The exact contribution from the electrons, and the exact contribution from the non-crossing ion orbits are retained in this approximation.

As we may see from Figs. 5 and 6, the piecewise-straight-line approximation agrees very well in both the small and the large ρ_i/δ cases with the exact solution. Even in the intermediate, $\rho_i/\delta = 1/10$ case, it is much better than the 3-region

approximation. The inclusion of the turning point contributions would make the agreement of the piecewise-straight-line approximation much better in all cases.

VI conclusions

We have calculated the exact growth rate, $\gamma(k)$, eigenfunctions, and effective potentials for the collisionless tearing mode in an anisotropic bi-Maxwellian neutral sheet by solving the integro-differential equation and using the exact particle orbits. The results are not qualitatively different than those reported earlier in the literature[1], although the best previous approximation, the 3-region approximation, under estimates the growth rate by a factor of two to five. We find that the presence of a favorable anisotropy ($T_{i\perp}/T_{i\parallel}$) greatly increases the growth rate and decreases the characteristic wavelength, especially in the case of $\rho_i/\delta \ll 1$.

When comparing the numerical integro-differential equation solution to the 3-region approximation for the isotropic tearing mode (see figs. 12 and 13) we found that the 3-region approximation breaks down in the small ρ_i regime. In this regime, the increase in the difference between the height of the effective potential in the electron inner region, and the adiabatic potential means that the eigenfunction is strongly evanescent inside of the electron inner region, and constant-ψ approximation of the 3-region approximation breaks down.

When an ion anisotropy was included, the difference between the three region approximation and the numerical solution of the integro-differential equation also increased. This is due primarily to the extension of the contribution of crossing ions to the potential for positions $\hat{z}$ outside of the ion-intermediate region which is due to high energy crossing ions,and to the break down of the local approximation in the ion intermediate region. In particular, for small ρ_i, the eigenmode becomes

deeply trapped in the ion-intermediate region as the ion anisotropy is increased, and therefore an approximation which assumes ψ is constant within the ion-intermediate region, such as the 3-region approximation, is contradictory.

We have also used a piecewise-straight-line approximation to solve the integro-differential equation in a simplified manner. This approximation allows quick evaluation of the matrix elements, facilitating the solution of the integro-differential equation, although it retains the essential features of the integro-differential treatment. In particular, this piecewise-straight-line approximation correctly classifies the orbits as crossing or non-crossing based on their value of momentum and energy rather than upon position, and assumes no particular form for the eigenfunction. This should be contrasted with the conventional straight-line and constant-ψ approximation in which all orbits within a given distance from the null plane are treated as straight-line orbits without distinguishing between crossing and non-crossing orbits and in which ψ is assumed to be constant near the null plane.

For our piecewise-straight-line approximation, we assumed that the velocity is constant over one basis function for ion crossing orbits. When a turning point occurred within a basis function, however, we ignored the contribution from that orbit. A further refinement to this approximation would be to include the turning point in some approximate fashion. In the large ρ_i limit, our approximation becomes exact since these crossing orbits are much larger than a basis function. Because in the small ρ_i limit, the region that the crossing orbits occupies is small, the details of particle orbits are not so important. Thus, in the small ρ_i limit the key aspect of

the piecewise-straight-line approximation is that is does not assume any particular form for the ψ eigenfunction.

acknowledgments

The authors would like to thank Y. C. Lee for a great deal of insight, and to J. F. Drake for discussions of the physics of the tearing instability. This work was funded by NASA.

References

[1] J. Chen and P. Palmadesso, *Phys. Fluids*, **27**, 1198, (1984).

[2] H. P. Furth, Nucl. Fusion Suppl. Pt. 1, 169, (1962).

[3] D. Pfirsch, *Z. Naturforsch Teil A*, **17**, 861, (1962).

[4] G. Laval and R. Pellat, *C. R. Acad. Sci. Paris*, **259**, 1706, (1964).

[5] G. Laval, R. Pellat and M. Vuillemin, in *Plasma Physics and Controlled Nuclear Fusion Research*, (IAEA, Vienna, 1966), *vol. 2*, p.259.

[6] B. Coppi, G. Laval and R. Pellat, *Phys. Rev. Letters*, **16**, 1207, (1966).

[7] K. Schindler, in *Proceedings of the Seventh International Conference on Phenomena in Ionized Gases*, (Gradevinska Knjiga, Beograd, Yugoslavia, 1966), vol. 2, p. 736; K. Schindler and M. Soop, *Phys. Fluids*, **11**, 1192, (1968).

[8] A. A. Galeev and L. M. Zelenyĭ, *Sov. Phys. JETP*, **43**, 1113, (1976).

[9] B. Lembage and R. Pellat, *Phys. Fluids*, **25**, 1995, (1982).

[10] W. Horton and T. Tajima, *J. Geophys. Research*, **93**, 2741, (1988).

[11] E. G. Harris, *Nuovo Cimento*, **23**, 115, (1962).

[12] N. F. Ness, *J. Geophys. Research*, **70**, 2989, (1965).

[13] A. Nishida, in *Magnetic Reconnection in Space and Laboratory Plasmas, Geophys. Monogr. Ser.*, edited by E. W. Hones, Jr., (AGU, Washington, D.C., 1984), vol. 30, p. 159.

[14] J. B. Greenly and B. U. Ö. Sonnerup, *J. Geophys. Research,* **86,** 1305, (1981).

[15] B. Quest, K. and F. V. Coroniti, *J. Geophys. Research,* **86,** 3289, ((1981)).

[16] D. W. Forslund, Ph.D. thesis, Princeton University (1968).

[17] G. Laval and R. Pellat, in *Proceedings of the ESRIN Study Group, Frascati, Italy,* (European Space Research Organization, Neuilly-sur-Seine, France, 1968), P. 5.

[18] B. Coppi and M. N. Rosenbluth, in *Proceedings of the ESRIN Study Group, Frascati, Italy,* (European Space Research Organization, Neuilly-sur-Seine, France, 1968), P.1.

[19] John Ambrosiano, Lou C. Lee, and Z. F. Fu, *J. Geophys. Research,* **91,** 113, (1986).

[20] G. S. Stiles, E. W. Hones,S. J. Bame, and J. R. Asbridge, *J. Geophys. Res.*, **83,** 3166, (1978).

[21] A. Nötzel, K. Schindler, and J. Birn, *J. Geophys. Res.*, **90,** 8293, (1985).

[22] J. Chen and P. J. Palmadesso, in *Magnetotail Physics,* edited by A. T. Y. Lui, (The Johns Hopkins University Press, Baltimore, MD, 1987) p. 321.

[23] J. Chen and P. J. Palmadesso, *J. Geophys. Res.*, **91**, 1499, (1986).

[24] J. P. Freidberg and R. L. Morse, *Phys. Fluids*, **12**, 887, (1969).

[25] M. Dobrowolny, *Nuovo Cimento B*, **55**, 427, (1968).

[26] J. Chen and Y. C. Lee, *Phys. Fluids*, **28**, 2137, (1985).

[27] J. Chen and Y. C. Lee, *Phys. Fluids*, **11**, 2944, (1988).

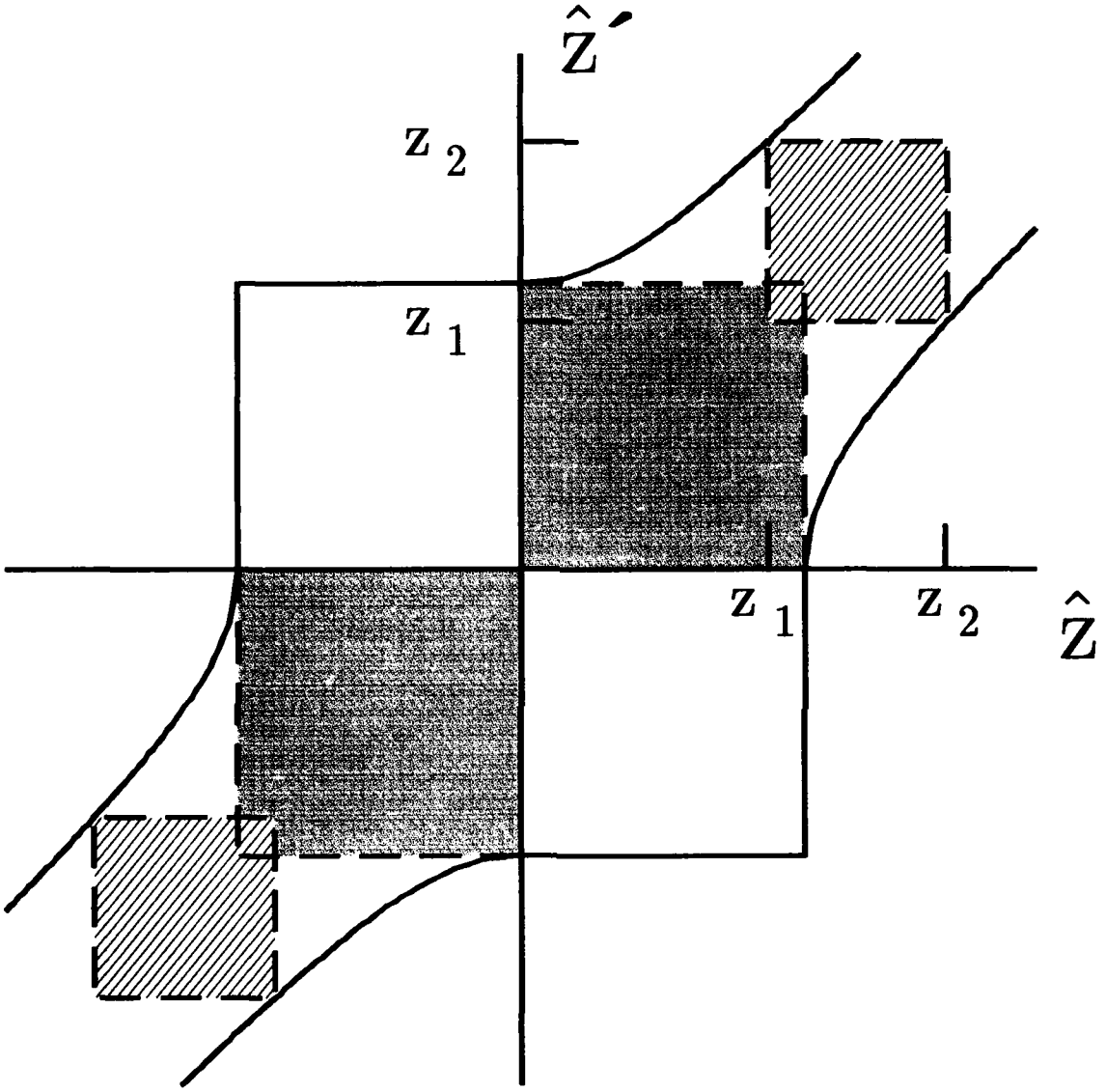

Figure 1. The region of integration for some non-crossing orbits. The gray shaded region is the region of integration for the non-crossing orbit with $p = -\sqrt{h}$, while the cross-hatched area is for an orbit with $p < -\sqrt{h}$.

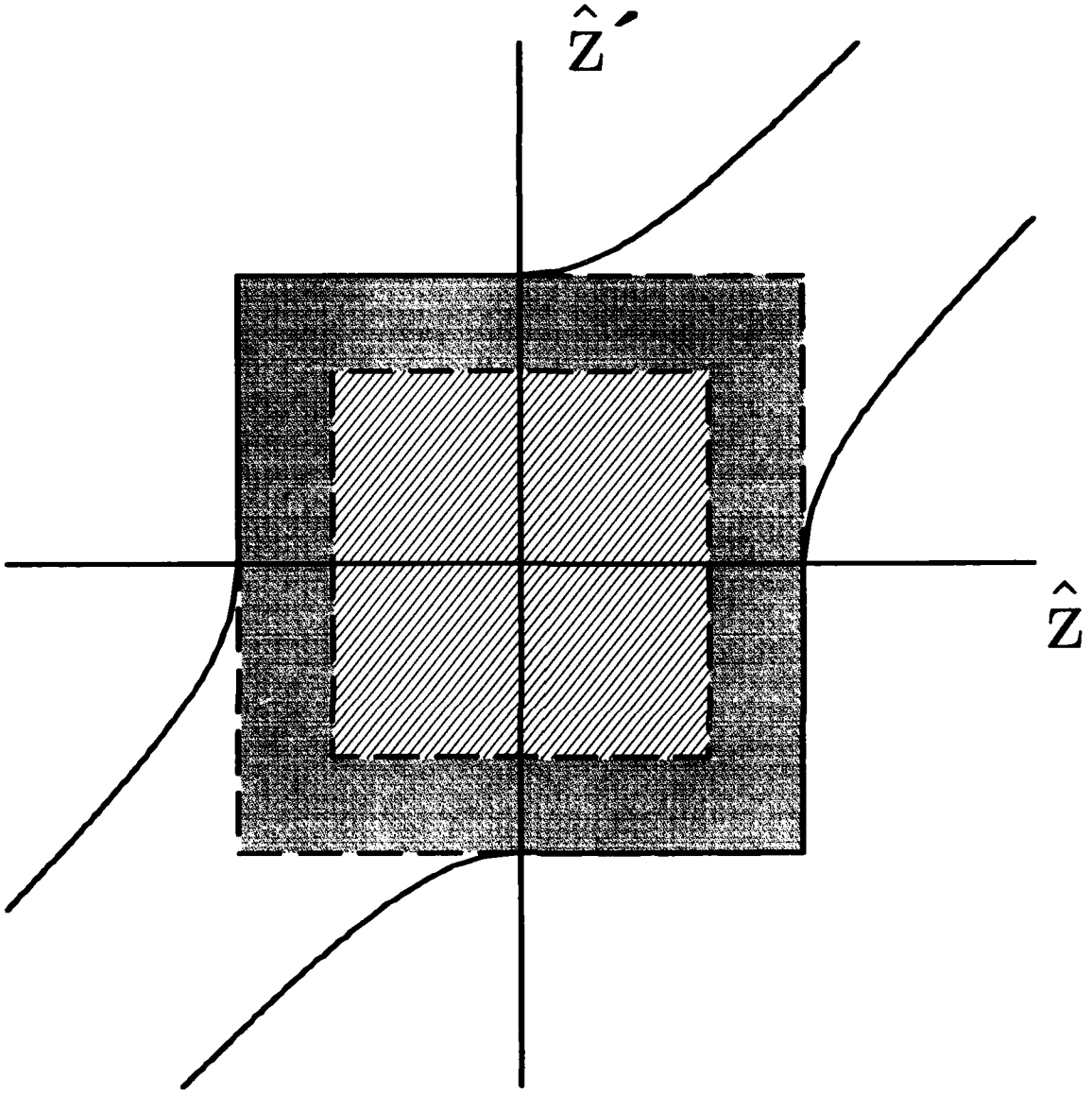

Figure 2. The region of integration for some crossing orbits. The gray region is the area of integration for the crossing orbit with the largest turning point, $p = -\sqrt{h}$. The cross-hatched region is for an orbit with smaller turning points, i.e. $p > -\sqrt{h}$.

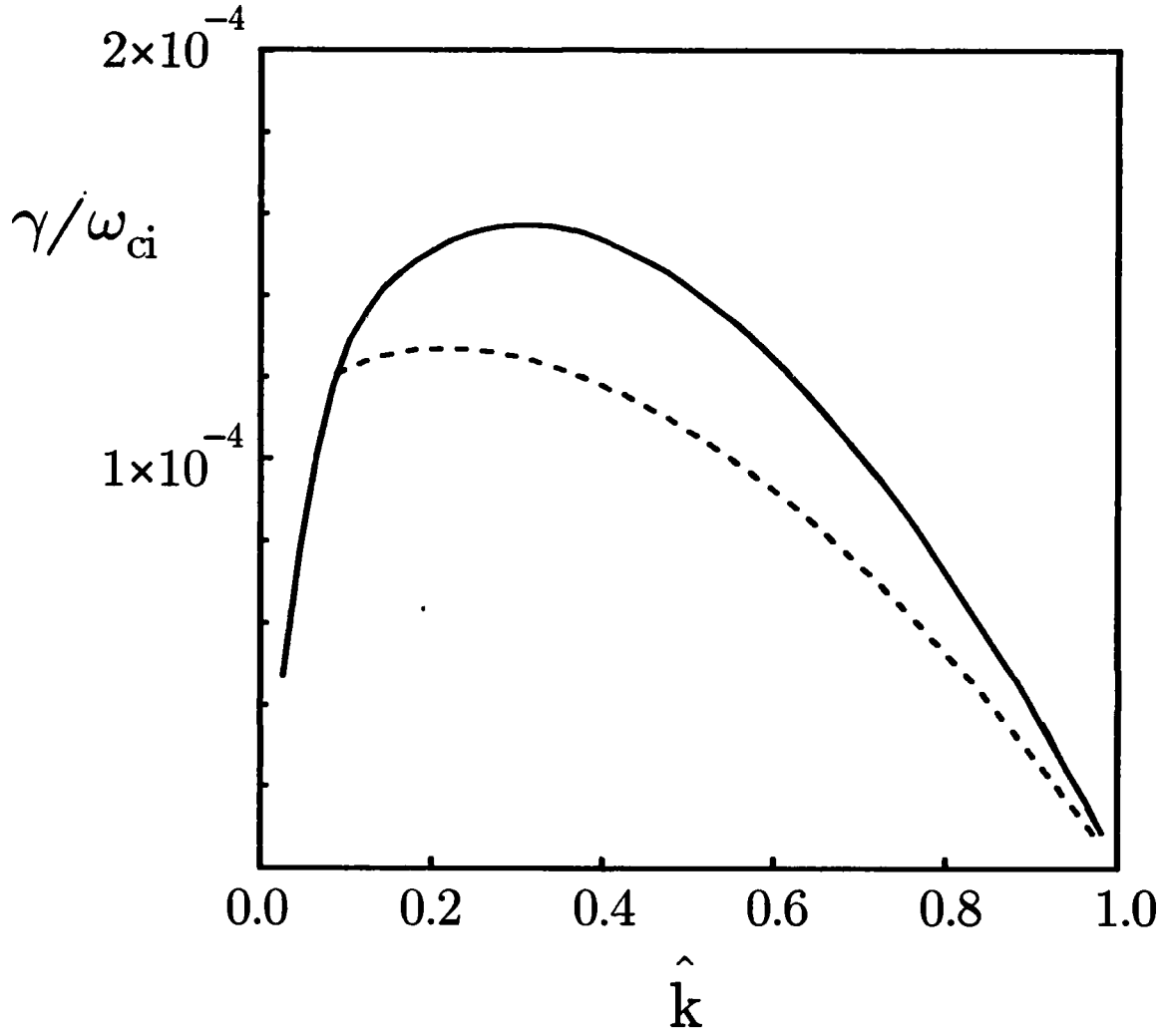

Figure 3. The growth rate vs. $\hat{k}$ for $\rho_i/\delta = 1/10$ and for the isotropic case, $T_{i\perp}/T_{i\parallel} = 1$. The short-dashed line is the 3-region approximation solution.

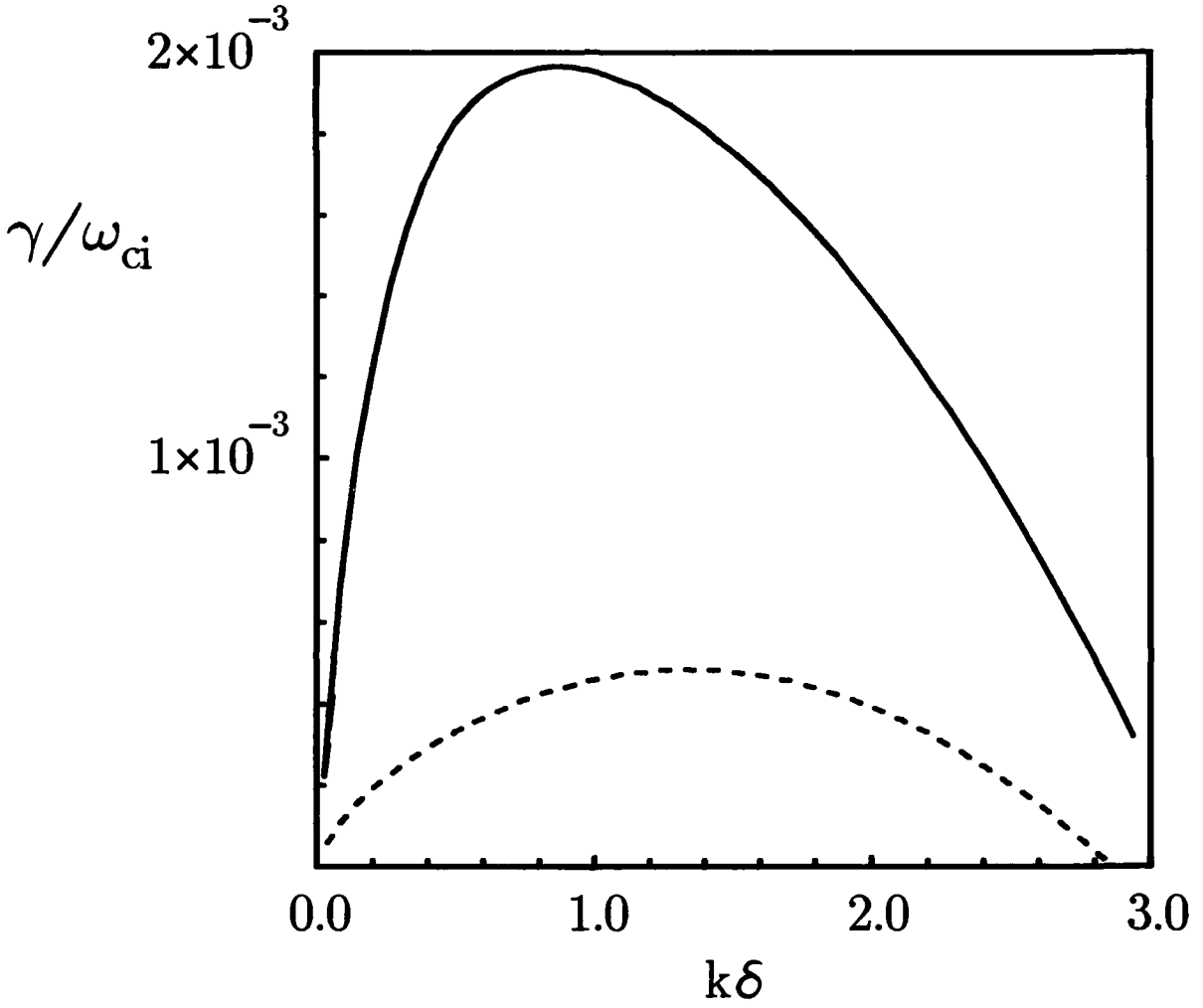

Figure 4. The growth rate vs. $\hat{k}$ for $\rho_i = 1/10$ and $T_{i\perp}/T_{i\|} = 1.2$. The short-dashed line is the 3-region approximation solution.

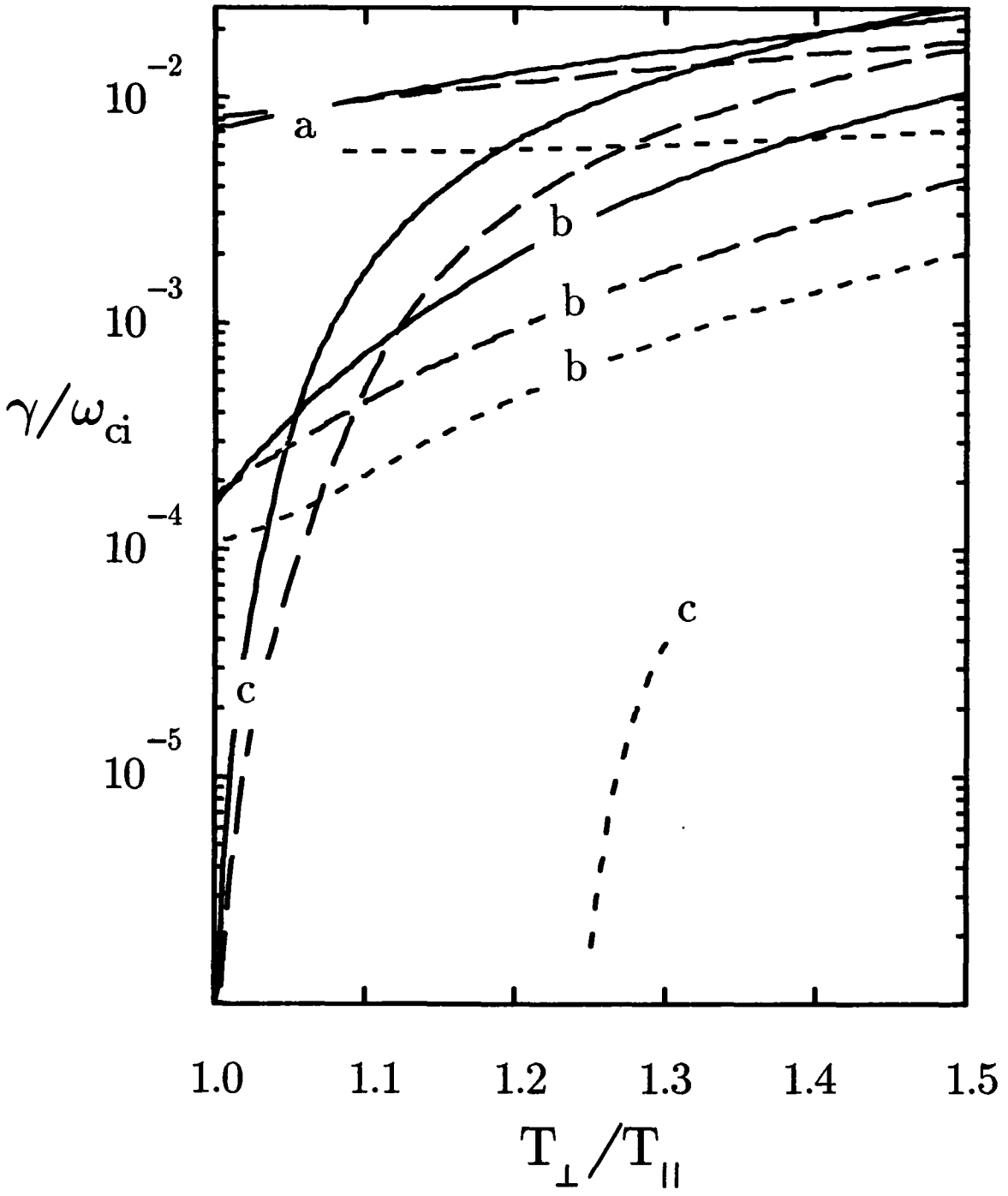

Figure 5. The peak growth rate as a function of ion anisotropy. "a", $\rho_i/\delta = 1/2$. "b", $\rho_i/\delta = 1/10$. "c", $\rho_i/\delta = 1/100$. The short dashes are the solution with the 3-region approximation, the long dashes are found using out piecewise-straight-line approximation, described in Sec. A.

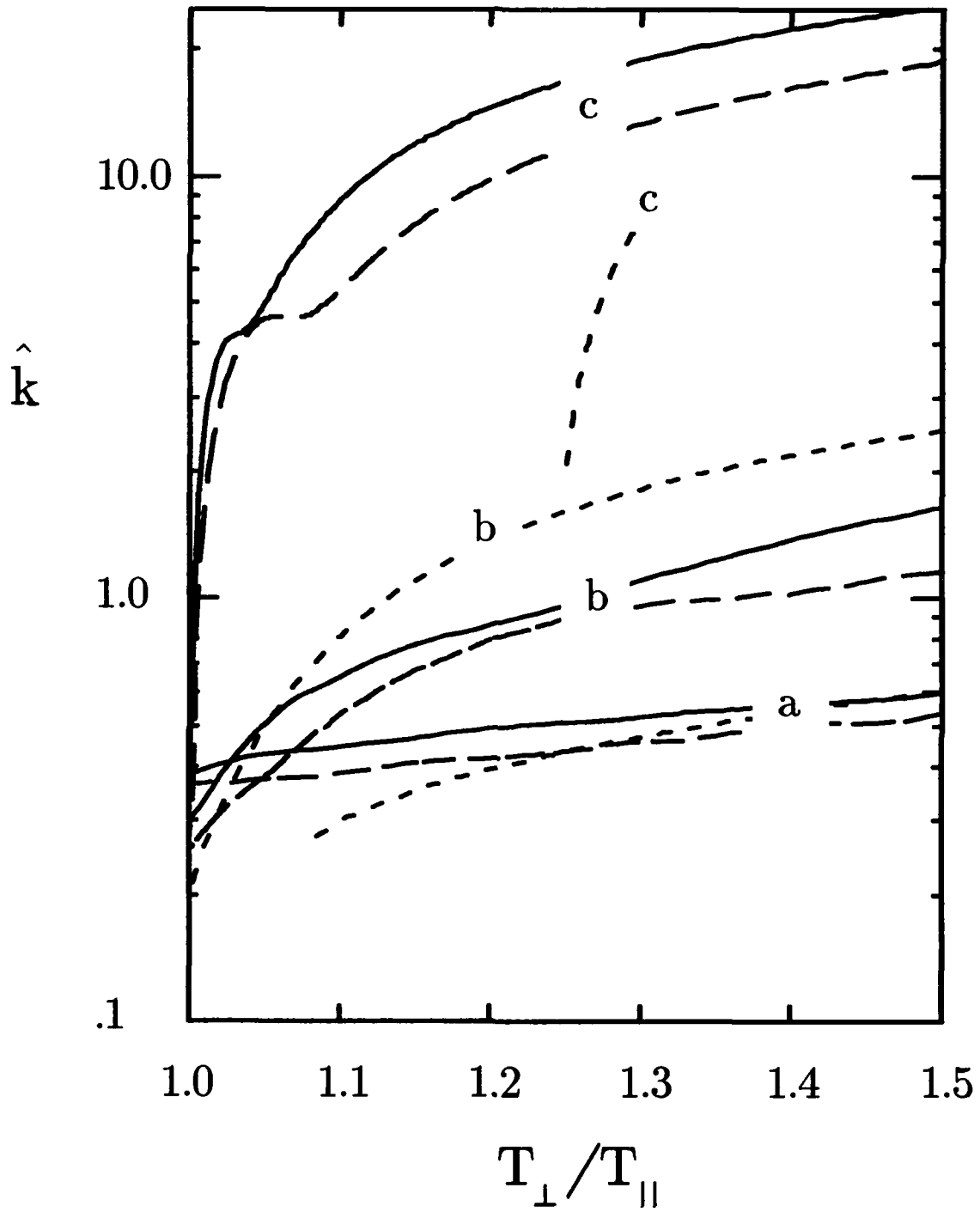

Figure 6. The wavenumbers corresponding to the peaks of the growth rate in Fig.9.

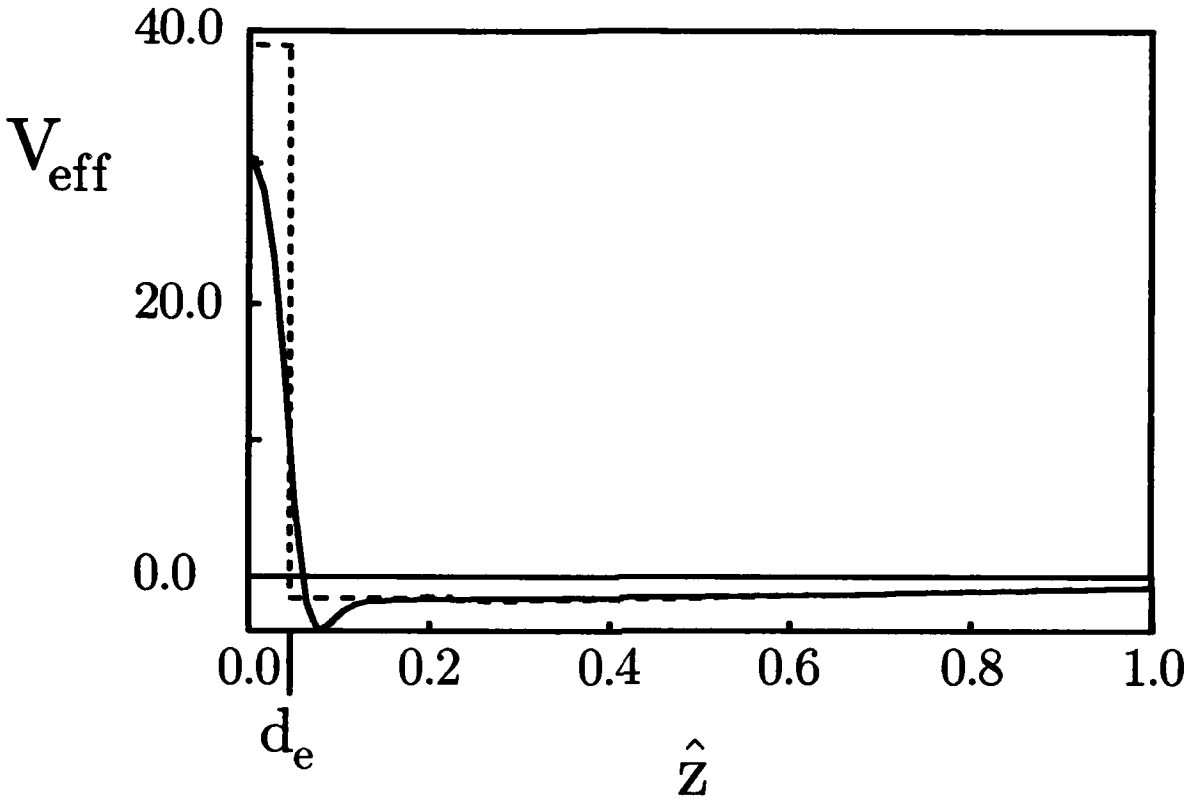

Figure 7. The effective potential well. The short dashes represent the 3-region approximation of Eq. (25). Parameters are $\rho_i/\delta = 1/10$, $T_{i\perp}/T_{i\parallel} = 1$, $\hat{k} = .5$, and $\gamma/\omega_{ci} = 1.43 \times 10^{-4}$.

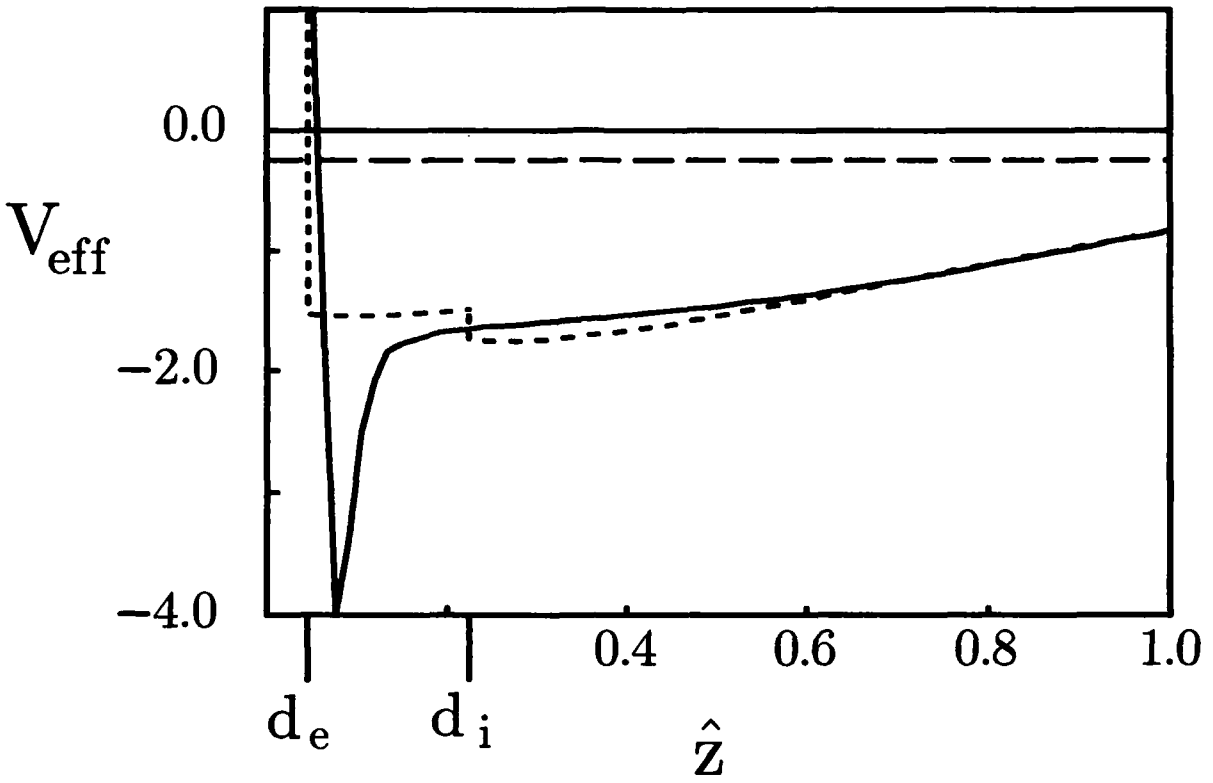

Figure 8. An enlargement of Fig. 3, showing the ion-intermediate region potential well.

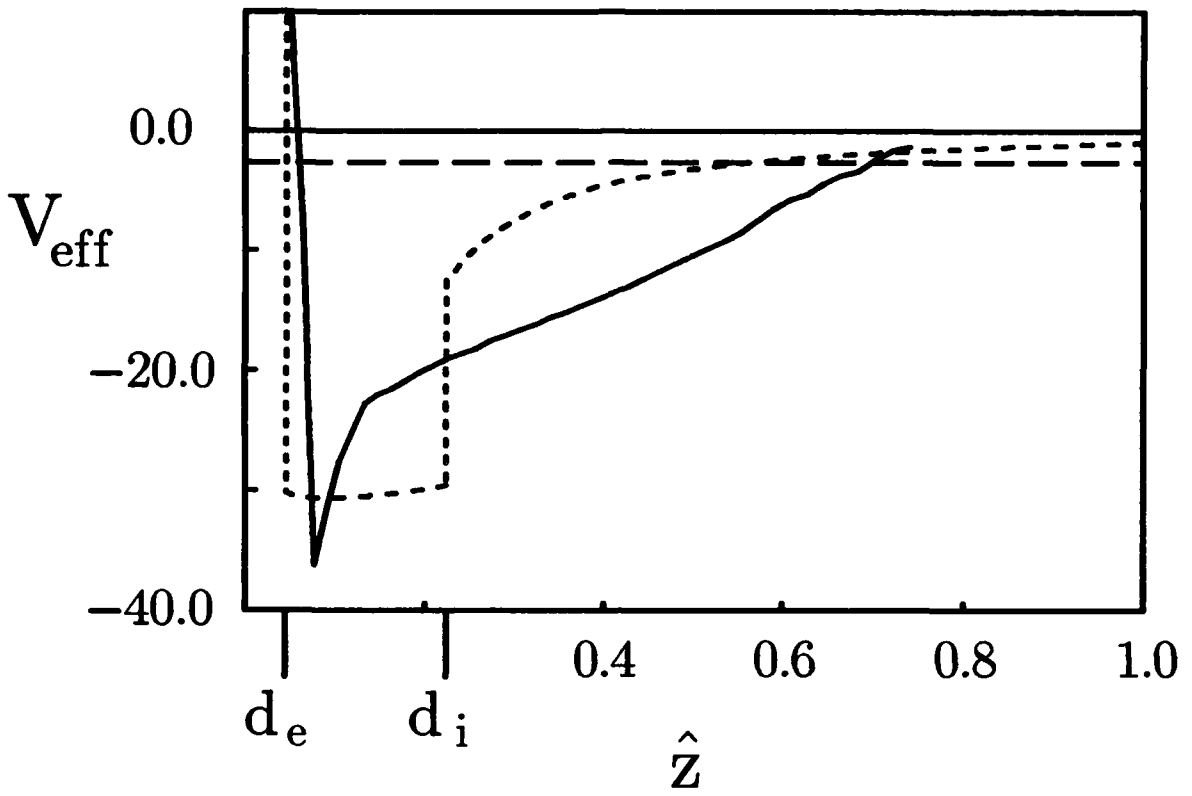

Figure 9. The effective potential well for $\rho_i/\delta = 1/10$ and $T_{i\perp}/T_{i\parallel} = 1.5$. $\hat{k} = 1.64$ and $\gamma/\omega_{ci} = 1.43 \times 10^{-2}$.

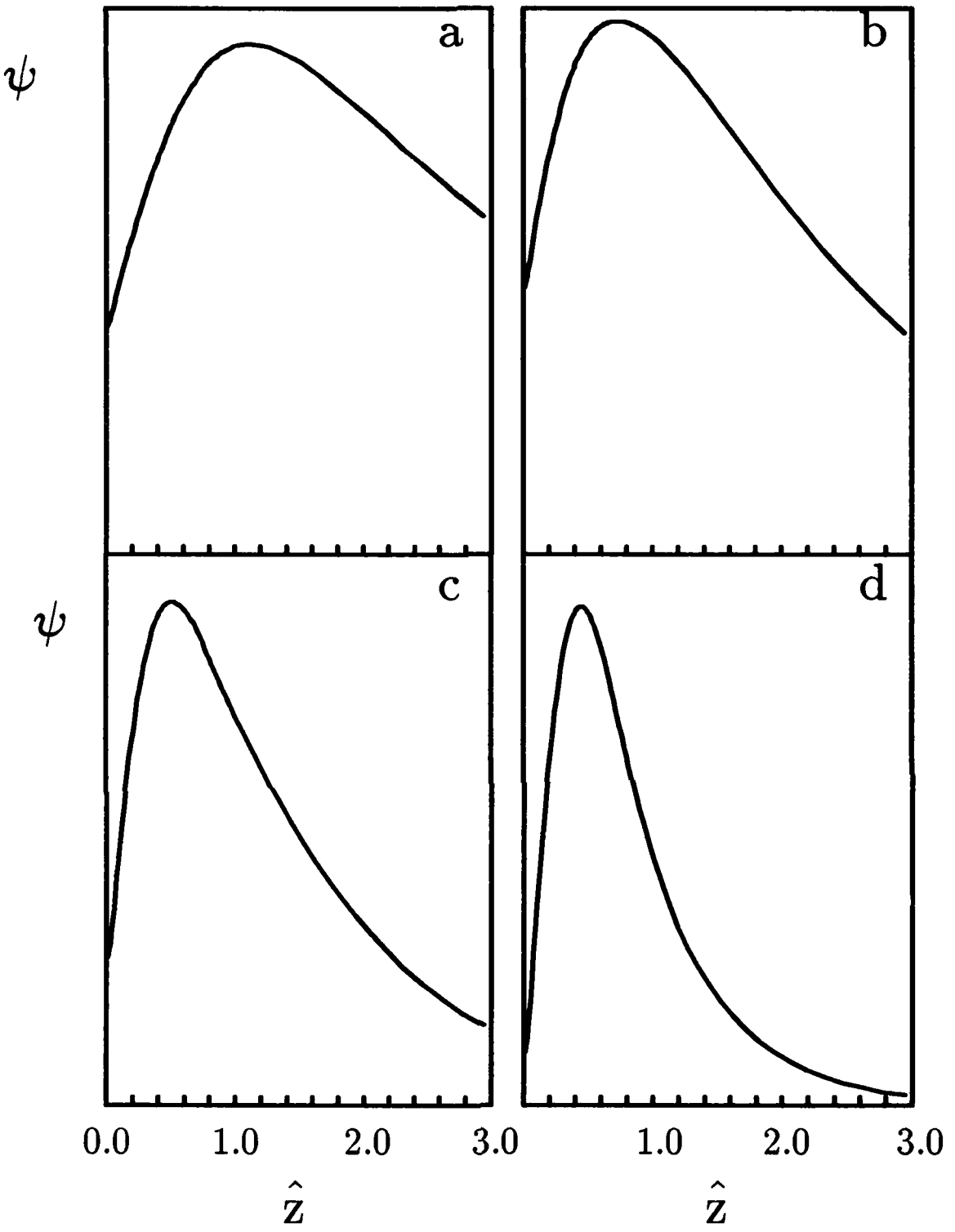

Figure 10. Eigenfunctions with $\rho_i/\delta = 1/10$. "a"; $T_{i\perp}/T_{i\|} = 1$, $\hat{k} = 0.31$ and $\gamma/\omega_{ci} = 1.58 \times 10^{-4}$. "b"; $T_{i\perp}/T_{i\|} = 1.05$, $\hat{k} = 0.52$ and $\gamma/\omega_{ci} = 3.74 \times 10^{-4}$. "c"; $T_{i\perp}/T_{i\|} = 1.2$, $\hat{k} = 0.86$ and $\gamma/\omega_{ci} = 1.96 \times 10^{-3}$. "d"; $T_{i\perp}/T_{i\|} = 1.5$, $\hat{k} = 1.64$ and $\gamma/\omega_{ci} = 1.44 \times 10^{-2}$. "b"; $T_{i\perp}/T_{i\|} = 1.05$, $\hat{k} = 0.52$ and $\gamma/\omega_{ci} = 3.74 \times 10^{-4}$.

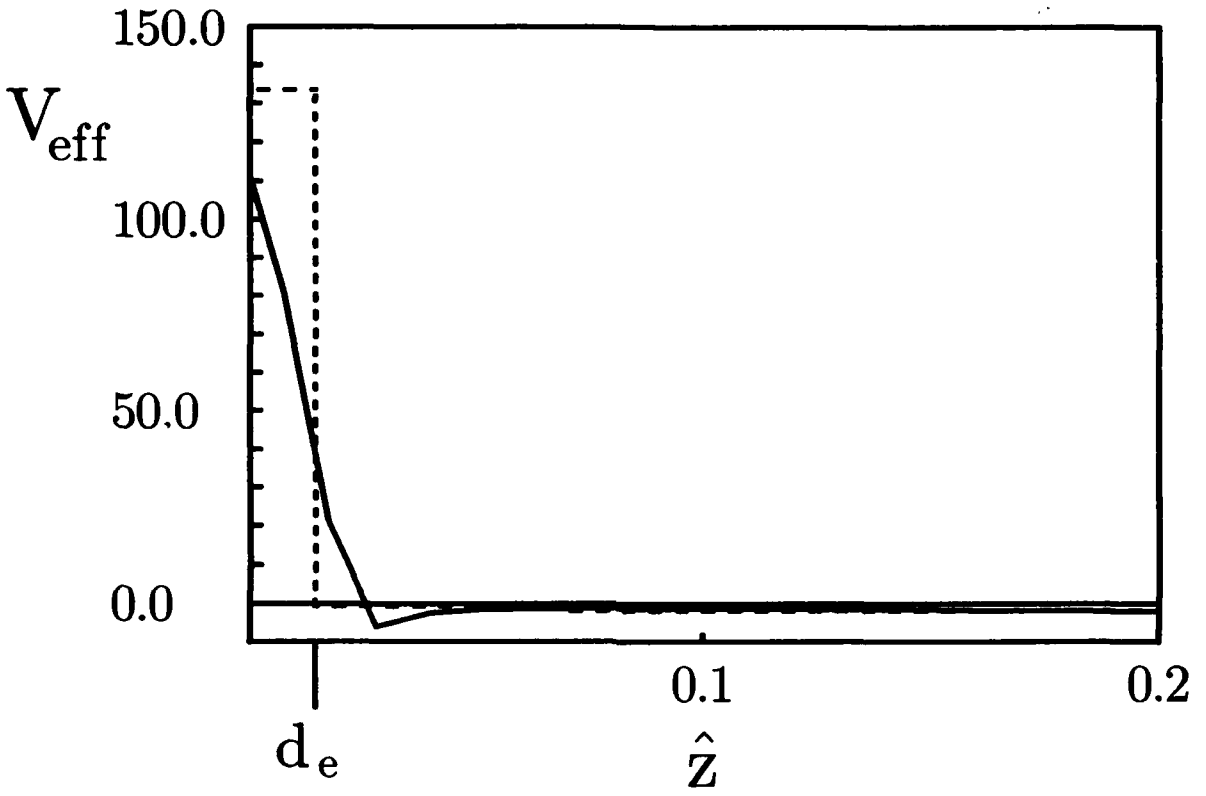

Figure 11. The effective potential well with $\rho_i/\delta = 1/100. T_{i\perp}/T_{i\|} = 1$, $\hat{k} = .5$, and $\gamma/\omega_{ci} = 4.74 \times 10^{-7}$.

DISTRIBUTION LIST
(Unclassified Only)

DISTRIBUTE ONE COPY EACH TO THE FOLLOWING PEOPLE (UNLESS OTHERWISE NOTED)

DIRECTOR
NAVAL RESEARCH LABORATORY
WASHINGTON, DC 20375-5000
CODE 4700 (26 CYS)
CODE 4701
CODE 4780 (50 CYS)
CODE 4750 (P. RODRIGUEZ)

OFFICE OF NAVAL RESEARCH
WASHINGTON, DC 22203
C. ROBERSON

DIRECTOR
DEFENSE NUCLEAR AGENCY
WASHINGTON, DC 20305
L. WITTWER
B. PRASAD

COMMANDING OFFICER
OFFICE OF NAVAL RESEARCH
WESTERN REGIONAL OFFICE
1030 EAST GREEN STREET
PASADENA, CA 91106
R. BRANDT

NASA HEADQUARTERS
CODE EE-8
WASHINGTON, DC 20546
S. SHAWHAN
D. BUTLER

NASA/GODDARD SPACE FLIGHT CENTER
GREENBELT, MD 20771
M. GOLDSTEIN, CODE 692
R.F. BENSON, CODE 692
T. NORTHROP, CODE 665
T. BIRMINGHAM, CODE 695.1
A. FIGUERO VINAS, CODE 692
SHING F. FUNG, CODE 696
D.S. SPICER, CODE 682

AEROSPACE CORPORATION
A6/2451, P.O. BOX 92957
LOS ANGELES, CA 90009
A. NEWMAN
D. GORNEY
M. SCHULZ
J. FENNEL

BELL LABORATORIES
MURRAY HILL, NJ 07974
A. HASEGAWA
L. LANZEROTTI

LAWRENCE LIVERMORE LABORATORY
UNIVERSITY OF CALIFORNIA
LIVERMORE, CA 94551
LIBRARY
B. KRUER
J. DEGROOT
B. LANGDON
R. BRIGGS
D. PEARLSTEIN

LOS ALAMOS NATIONAL LABORATORY
P.O. BOX 1663
LOS ALAMOS, NM 87545
S.P. GARY
N. QUEST
J. BRACKBILL
J. BIRN
J. BOROVSKY
D. FORSLUND
B. BEZZERIDES
C. NIELSON
D. RIGGIN
D. SIMONS
L. THODE
D. WINSKE

LOCKHEED RESEARCH LABORATORY
PALO ALTO, CA 94303
M. WALT
J. CLADIS
Y. CHIU
R. SHARP
E. SHELLEY

NATIONAL SCIENCE FOUNDATION
ATMOSPHERIC RESEARCH SECTION
WASHINGTON, DC 20550
D. PEACOCK

PHYSICAL INTERNATIONAL CORP.
2400 MERCED STREET
SAN LEANDRO, CA 94557
J. BENFORD
S. STALINGS
Y. YOUNG

SANDIA LABORATORIES
ALBUQUERQUE, NM 87115
A. TOEPFER
D. VANDEVENDER
J. FREEMAN
T. WRIGHT

SCIENCE APPLICATIONS
INTERNATIONAL CORPORATION
LAB. OF APPLIED PLASMA STUDIES
P.O. BOX 2351
LAJOLLA, CA 92037
L. LINSON

TRW SPACE AND TECHNOLOGY GROUP
SPACE SCIENCE DEPARTMENT
BUILDING R-1, ROOM 1170
ONE SPACE PARK
REDONDO BEACH, CA 90278
R. FREDERICKS
W.L. TAYLOR

UNIVERSITY OF ALASKA
GEOPHYSICAL INSTITUTE
FAIRBANKS, AK 99701
LIBRARY
S. AKASOFU
J. KAN
J. ROEDERER
L. LEE
D. SWIFT

UNIVERSITY OF ARIZONA
DEPT. OF PLANETARY SCIENCES
TUCSON, AZ 85721
J.R. JOKIPII

BOSTON COLLEGE
DEPARTMENT OF PHYSICS
CHESTNUT HILL, MA 02167
R.L. CAROVILLANO
P. BAKSHI

UNIVERSITY OF CALIFORNIA, S.D.
LAJOLLA, CA 92037
(PHYSICS DEPARTMENT):
T. O'NEIL
J. WINFREY
LIBRARY
J. MALMBERG
(DEPT. OF APPLIED SCIENCES):
H. BOOKER

UNIVERSITY OF CALIFORNIA
SPACE SCIENCE LABORATORY
BERKELEY, CA 94720
M. TEMERIN
F. MOZER

UNIVERSITY OF CALIFORNIA
PHYSICS DEPARTMENT
IRVINE, CA 92664
LIBRARY
G. BENFORD
N. ROSTOKER
C. ROBERTSON
N. RYNN

UNIVERSITY OF CALIFORNIA
LOS ANGELES, CA 90024
(PHYSICS DEPARTMENT):
J.M. DAWSON
B. FRIED
J. MAGGS
J.G. MORALLES
W. GEKELMAN
R. STENZEL
Y. LEE
A. WONG
F. CHEN
M. ASHOUR-ABDALLA
LIBRARY
J.M. CORNWALL
R. WALKER
P. PRITCHETT
(INSTITUTE OF GEOHPYSICS
AND PLANETARY PHYSICS):
LIBRARY
C. KENNEL
F. CORONITI

UNIVERSITY OF CHICAGO
ENRICO FERMI INSTITUTE
CHICAGO, IL 60637
E.N. PARKER
I. LERCHE
LIBRARY

UNIVERSITY OF COLORADO
DEPT. OF ASTRO-GEOPHYSICS
BOULDER, CO 80302
M. GOLDMAN
LIBRARY

CORNELL UNIVERSITY
SCHOOL OF APPLIED AND
ENGINEERING PHYSICS
COLLEGE OF ENGINEERING
ITHACA, NY 14853
LIBRARY
R. SUDAN
R. KUSSE
M. FLEISCHMANN
C. WHARTON
F. MORSE
R. LOVELACE
P.M. KINTNER

HARVARD UNIVERSITY
CENTER FOR ASTROPHYSICS
60 GARDEN STREET
CAMBRIDGE, MA 02138
G.B. FIELD
R. ROSNER
K. TSINGANOS
G.S. VAIANA

UNIVERSITY OF IOWA
IOWA CITY, IA 52240
C.K. GOERTZ
D. GURNETT
G. KNORR
D. NICHOLSON
C. GRABBE
L.A. FRANK
K. NISHIKAWA
N. D'ANGELO
R. MERLINO
C. HUANG

UNIVERSITY OF MARYLAND
PHYSICS DEPARTMENT
COLLEGE PARK, MD 20742
K. PAPADOPOULOS
H. ROWLAND
C. WU

UNIVERSITY OF MARYLAND, IPST
COLLEGE PARK, MD 20742
DAVID MATTHEWS

UNIVERSITY OF MINNESOTA
SCHOOL OF PHYSICS
MINNEAPOLIS, MN 55455
LIBRARY
J.R. WINCKLER
P. KELLOGG
R. LYSAK

M.I.T.
CAMBRIDGE, MA 02139
LIBRARY
(PHYSICS DEPARTMENT):
B. COPPI
V. GEORGE
G. BEKEFI
T. CHANG
T. DUPREE
R. DAVIDSON
(ELECTRICAL ENGINEERING
DEPARTMENT):
R. PARKER
A. BERS
L. SMULLIN
(R.L.E):
LIBRARY
(SPACE SCIENCE):
READING ROOM

UNIVERSITY OF NEW HAMPSHIRE
DEPARTMENT OF PHYSICS
DURHAM, NH 03824
R.L. KAUFMAN
J. HOLLWEG

PRINCETON UNIVERSITY
PRINCETON, NJ 08540
PHYSICS LIBRARY
PLASMA PHYSICS LAB. LIBRARY
F. PERKINS
T.K. CHU
H. OKUDA
H. HENDEL
R. WHITE
R. KURLSRUD
H. FURTH
S. YOSHIKAWA
P. RUTHERFORD

RICE UNIVERSITY
HOUSTON, TX 77001
SPACE SCIENCE LIBRARY
T. HILL
R. WOLF
P. REIFF
G.-H. VOIGT

UNIVERSITY OF ROCHESTER
ROCHESTER, NY 14627
A. SIMON

STANFORD UNIVERSITY
RADIO SCIENCE LABORATORY
STANFORD, CA 94305
R. HELLIWELL

STEVENS INSTITUTE OF TECHNOLOGY
HOBOKEN, NJ 07030
B. ROSEN
G. SCHMIDT
M. SEIDL

UNIVERSITY OF TEXAS
AUSTIN, TX 78712
W. DRUMMOND
V. WONG
D. ROSS
W. HORTON

UNIVERSITY OF TEXAS
CENTER FOR SPACE SCIENCES
P.O. BOX 688
RICHARDSON, TX 75080
DAVID KLUMPAR

THAYER SCHOOL OF ENGINEERING
DARTMOUTH COLLEGE
HANOVER, NH 03755
BENGT U.O. SONNERUP
M. HUDSON

UTAH STATE UNIVERSITY
DEPT. OF PHYSICS
LOGAN, UT 84322
ROBERT W. SCHUNK

UNIVERSITY OF THESSALONIKI
DEPARTMENT OF PHYSICS
GR-54006 THESSALONIKI,
GREECE
L. VLAHOS